## REVIEW

Check for updates

# Multi-scale structural design of electromagnetic wave absorbers: pathways to improved performance

Yang Guan,[abc] Yongpeng Wu,[a] Jianyu Zhou,[a] Kai Yao,[a] Ruolin Liu,[a] Yang Yang*[a] and Wei Lu [ID] *[a]

With the rapid advancement of wireless communication technologies and the proliferation of Internet of Things (IoT) devices over the past decade, electromagnetic interference (EMI) has emerged as a significant challenge. EMI can degrade the performance, stability, and lifespan of advanced electronics and even poses potential health risks. One of the most effective strategies to mitigate this issue is the development of highly efficient electromagnetic wave absorbers (EMAs), a field that has garnered considerable attention. However, achieving the necessary efficiency for widespread adoption remains a challenge. The internal structure of EMAs plays a pivotal role in determining their absorption performance. This review explores the fundamental principles of electromagnetic wave absorption and highlights recent advancements in optimizing internal structures across various length scales, from the atomic to the macroscopic level. We examine design strategies, structure–performance relationships, and fabrication methods for tuning absorption efficiency, either independently or in combination. Finally, we address key challenges and future directions for the next generation of EMAs, offering insights into their potential for practical applications.

### Wider impact

This review focuses on the significant progress in the multi-scale structural design of electromagnetic wave absorbers (EMAs), highlighting the breakthroughs in enhancing their absorption performance. The research covers the atomic/molecular scale, nanoscale, microscale, and macroscale. Multi-scale structural design plays a decisive role in determining the electromagnetic parameters, impedance matching characteristics, and loss mechanisms of materials, providing a broad design space for breaking through the physical limits of traditional materials in terms of "thinness, lightness, wideband, and strength" performance. These breakthroughs are crucial for advancing the research on intelligent and integrated EMAs and offer innovative solutions to address the increasingly severe demands of electromagnetic interference (EMI) and radar stealth. Through the study of multi-scale structural design of EMAs, this review has made important contributions to the development of advanced EMAs to alleviate electromagnetic pollution.

## 1. Introduction

With the rapid development of 6G mobile communication technology, the Internet of Things (IoT) and artificial intelligence (AI) technology, the extensive application of electromagnetic waves (EMWs) in wireless communication, radar detection and electronic devices has made the problem of electromagnetic interference (EMI) increasingly prominent.

[a] Shanghai Key Lab. of D&A for Metal-Functional Materials, School of Materials Science & Engineering, Tongji University, Shanghai 201804, China.
E-mail: yangyang_@tongji.edu.cn, weilu@tongji.edu.cn
[b] Shanghai Institute of Ceramics, Chinese Academy of Sciences, Shanghai 200050, China
[c] University of the Chinese Academy of Sciences, Beijing 100049, China

EMI adversely impacts the reliable functioning of electronic devices, resulting in diminished efficiency, and also presents possible health hazards to humans.[1,2] Meanwhile, in the military field, the application of precision-guided technology has driven the rapid development of radar stealth technology.[3] Therefore, the development and application of new multifunctional EMAs have become some of the important study directions in current scientific studies across various countries.[4] Excellent EMAs must fulfill criteria of having minimal thickness, light weight, robust absorption, and broad frequency band, while also ensuring anti-oxidation, corrosion resistance, high-temperature resistance and environmental friendliness.[5,6] In recent years, to enhance the overall performance of EMAs, researchers have concentrated on the structural design of these materials and conducted significant

investigations into the correlation between the structure and performance.[7,8]

Over the past several decades, tremendous progress has been achieved in the research of EMAs, and the related technology development has shown a vigorous trend.[9,10] On the basis of the various loss mechanisms of EMAs, traditional EMAs can mainly be classified into three types: dielectric loss type,[11,12] resistive loss type,[13] and magnetic loss type materials.[14,15] Dielectric loss type EMAs include ceramic materials (e.g., SiC, $BaTiO_3$) and polymer composites.[16,17] These materials exhibit superior high-frequency absorption performance, outstanding high-temperature resistance and excellent chemical stability.[18] However, they suffer from certain limitations, including difficulties in dielectric constant regulation, and for some ceramic materials, notable brittleness and poor processability.[19] Resistive loss type EMAs primarily include graphene,[20,21] and carbon nanotubes (CNTs).[22,23] These materials demonstrate promising broadband absorption capabilities, widely tunable electrical conductivity and excellent potential for functionalization modifications.[24] However, they are prone to severe agglomeration and frequently demonstrate unsatisfactory impedance matching performances.[25] Magnetic loss type EMAs primarily consist of ferrites, metallic magnetic powders and their alloys.[26] These materials typically exhibit strong absorption intensity and low-cost advantages, but their practical applications are significantly limited by high density and susceptibility to corrosion. However, as the requirements for thin, light, wide, and strong absorption become increasingly strict, material design based solely on chemical composition modulation has become increasingly unable to meet the needs of practical applications.[27,28] The fundamental challenge lies in the inherent trade-off between impedance matching and attenuation capacity, which is difficult to decouple within a single chemical composition modulation. Therefore, shifting the design paradigm from composition-driven to structure-driven through multi-scale structural design is no longer just an option, but a necessity.[29,30]

Multi-scale structural designs of EMAs include atomic/molecular scale, nanoscale, microscale and macroscale designs.[31] Through the design of multi-scale structures, EMAs can exhibit unique structures and properties, effectively regulating EMW absorption, and providing an effective approach for constructing broadband EMAs.[32] In particular, atomic/molecular scale design includes an atomic dispersion system,[33] and defect engineering.[34,35] At this scale, it is possible to precisely control the intrinsic electromagnetic parameters of materials, and by designing defects and sites, one can actively create the desired physical mechanisms. In addition, nanoscale design encompasses the regulation of nanostructure morphology,[36] and the design of low-dimensional nanomaterials.[37] By constructing a hollow structure,[38] porous structure,[39] and core–shell structure,[40] the morphology of nanostructures can be controlled, and this can enrich the attenuation mechanisms of EMAs. Low-dimensional nanomaterials can enhance the dielectric loss capacity of EMAs. Furthermore, the microscale design includes designs such as aerogels,[41] porous foams,[42] fiber

network materials,[43] layered structures,[44] and oriented arrangement structures. This scale solves the problems of traditional materials' tendency to agglomerate and their single functionality, and endows the materials with lightweight and high-loss properties. Additionally, the macroscale design includes periodic arrays,[158] frequency-selective surfaces (FSSs),[160] and impedance gradient regulation.[162] Macroscale design no longer merely focuses on the chemical composition of the material itself; instead, it constructs macroscopic physical structures to manage and control EMWs, thereby achieving breakthroughs in EMW absorption performance.

This work systematically reviews the latest progress in the multi-scale structural design of EMAs. This paper initially introduces the basic principles of EMW absorption, then provides a comprehensive overview of EMAs with different scale structure types; layer by layer, it analyzes the structural design strategies from the atomic scale to the macro scale and how their regulation affects performance; finally, in view of the challenges faced by EMAs in some emerging application scenarios, the future development direction of broadband EMAs is discussed. This review aims to provide theoretical guidance for the development of the next generation of intelligent tunable, wideband and efficient EMAs (Fig. 1).

## 2. EMW absorption theory

The core of EMW absorption theory lies in investigating how to maximize the conversion of incident EMW energy into other forms of energy through specific absorbers, thereby reducing or eliminating the reflection and transmission of EMWs.[45] The performance of EMAs is directly dictated by the degree of impedance matching between the absorber and free space, as well as the absorber's own electromagnetic loss capability.[46]

When EMWs interact with EMAs, it can be described based on Maxwell's equations: when the EM field oscillates with the EMAs, a relative response is generated, leading to energy dissipation of the EMAs.[47] Maxwell's equations reveal the constitutive relationship between EMAs and EMWs. Their response characteristics are jointly described by complex permittivity ($\varepsilon_r$) and complex permeability ($\mu_r$), and these complex parameters comprehensively manifest the electromagnetic energy storage and dissipation characteristics of EMAs. The formulas for $\varepsilon_r$ and $\mu_r$ are as follows:[48,49]

$$\varepsilon_r = \varepsilon' - j\varepsilon'' \tag{1}$$

$$\mu_r = \mu' - j\mu'' \tag{2}$$

where the real part of the dielectric constant ($\varepsilon'$) and the imaginary part of the dielectric constant ($\varepsilon''$) respectively represent the storage and dissipation capabilities of electric energy, while the real part of the magnetic permeability ($\mu'$) and the imaginary part of the magnetic permeability ($\mu''$) respectively represent the storage and dissipation capabilities of magnetic energy.[50]
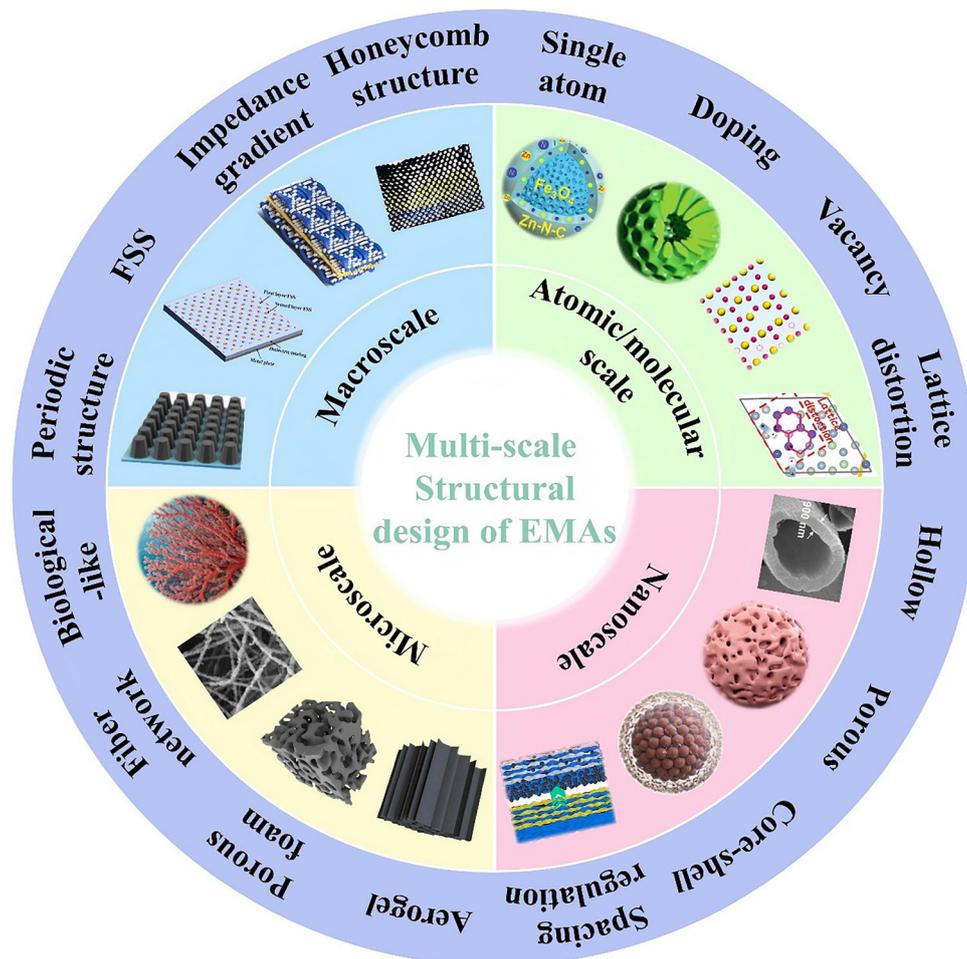
**Fig. 1** Multi-scale structural design of EMAs, including design strategies at atomic/molecular scale, nanoscale, microscale, and macroscale. Images for atomic/molecular scale: reproduced with permission from ref. 93. Copyright (2021) John Wiley and Sons; reproduced with permission from ref. 103. Copyright (2026) Elsevier; reproduced with permission from ref. 109. Copyright (2023) Elsevier; reproduced with permission from ref. 114. Copyright (2024) John Wiley and Sons. Images for nanoscale: reproduced with permission from ref. 117. Copyright (2020) Elsevier; reproduced with permission from ref. 123. Copyright (2025) Elsevier; reproduced with permission from ref. 137. Copyright (2023) Elsevier; reproduced with permission from ref. 150. Copyright (2023) Springer Nature. Images for microscale: reproduced with permission from ref. 153. Copyright (2023) Elsevier; reproduced with permission from ref. 155. Copyright (2025) Elsevier; reproduced with permission from ref. 157. Copyright (2025) Elsevier; reproduced with permission from ref. 163. Copyright (2025) Elsevier. Images for macroscale: reproduced with permission from ref. 168. Copyright (2024) John Wiley and Sons; reproduced with permission from ref. 169. Copyright (2017) Elsevier; reproduced with permission from ref. 174. Copyright (2023) Elsevier; reproduced with permission from ref. 176. Copyright (2024) Donghua University.

## 2.1. Electromagnetic absorption performance evaluation

Compared to electromagnetic shielding materials, EMAs generate less secondary pollution when processing EMWs. The key indicator for evaluating the performance of EMAs is reflection loss (RL).[51] A more negative RL value indicates a stronger absorption capability. Typically, RL $\leq$ −10 dB (which refers to a 90% absorption rate) is considered effective absorption, while RL $\leq$ −20 dB (99% absorption rate) indicates exceptional performance.[52] The effective absorption bandwidth (EAB), which corresponds to the frequency range where RL $\leq$ −10 dB, serves as another crucial metric for evaluating the performance of EMAs. Modern applications urgently require EMAs to possess a wider EAB. According to transmission line theory, RL can

be calculated using the following formulas:[53,54]

$$\text{RL (dB)} = 20 \lg \left| \frac{Z_{\text{in}} - Z_0}{Z_{\text{in}} + Z_0} \right| \quad (3)$$

$$Z_{\text{in}} = Z_0 \sqrt{\frac{\mu_{\text{r}}}{\varepsilon_{\text{r}}}} \tanh \left[ j \left( \frac{2\pi f d}{c} \right) \sqrt{\mu_{\text{r}} \varepsilon_{\text{r}}} \right] \quad (4)$$

where $Z_0$ represents the air impedance, $Z_{\text{in}}$ signifies the input impedance of EMAs, $d$ is the thickness of the EMAs, $c$ represents the velocity of light in free space, and $f$ is the frequency, respectively. The closer the $Z$ value is to 1, that is, when the $Z_{\text{in}}$ of the EMAs is nearer the $Z_0$, the more easily the EMWs can enter the interior of the EMAs.[55] This phenomenon is called

impedance matching. When the $Z$ value is equal to 1, at this time, the EMWs can pass through the EMAs completely without reflection, forming perfect impedance matching.[56]

The recently proposed delta function method in research offers an innovative solution for the assessment of electromagnetic impedance matching degree, and the formula is as follows:[57]

$$|\Delta| = |\sinh^2(Kfd) - M| \qquad (5)$$

where $K$ and $M$ can be determined by the complex permittivity and permeability. For this equation, it can be seen that as the delta value approaches 0, it indicates good impedance matching and superior EMW absorption performance. Conversely, as $|\Delta|$ moves away from 0, it leads to poor impedance matching and inferior EMW absorption performance.[58]

## 2.2. EMW attenuation mechanisms

The attenuation mechanism of EMAs is the core physical basis. The attenuation mechanism can mainly be divided into two categories: dielectric loss and magnetic loss.[59] The detailed attenuation mechanisms of EMW absorption are shown in Fig. 2. The dielectric loss tangent ($\tan \delta_e = \varepsilon''/\varepsilon'$) and the magnetic loss tangent ($\tan \delta_m = \mu''/\mu'$) can be used to evaluate the dielectric loss and magnetic loss capabilities, respectively.[60] Different attenuation mechanisms determine the way in which EMAs convert the energy of EMWs into other forms of energy and dissipate it.

**2.2.1. Dielectric loss.** Dielectric loss is mainly caused by the material's polarization relaxation and carrier migration in response to alternating electric fields. According to the Debye theory, dielectric loss is mainly composed of conductive loss and polarization loss.[61] Based on Maxwell's equations and the Debye theory, $\varepsilon''$ can be expressed by the following equation:[62]

$$\varepsilon'' = \varepsilon_p'' + \varepsilon_c'' = \frac{2\pi f \tau (\varepsilon_s - \varepsilon_\infty)}{1 + (2\pi f)^2 \tau^2} + \frac{\sigma}{2\pi f \varepsilon_0} \qquad (6)$$

where $\tau$ is the polarization relaxation time, $\sigma$ is the electrical conductivity, $\varepsilon_0$ is the vacuum dielectric constant, $\varepsilon_s$ stands for the optical permittivity and $\varepsilon_\infty$ is the static permittivity, respectively.

Conductive loss refers to the process where the charge carriers within the material undergo directional migration under the alternating electric field of the incident EMWs, forming an electric current. The material's own resistance causes Joule heating during the current flow, thereby converting the electromagnetic energy into thermal energy.[63] High conductivity EMAs have a high electrical conductivity, so the $\varepsilon''$ value is also high, indicating strong dielectric loss. However, high conductivity can lead to poor impedance matching and a decline in EMW absorption performance.[64,65]

Polarization loss refers to the phenomenon where the electric dipoles in a material will shift and rearrange under the influence of an alternating electric field, attempting to keep up with the changes in the direction of the electric field.[66] However, this polarization process lags behind the changes in the electric field, and this lag results in the dissipation of energy in the form of heat.[67] Compared to conductive loss, polarization loss has more manifestations, specifically including interface polarization, dipole polarization, electron polarization and ionic polarization.[68] However, electron polarization and dipole polarization usually occur in the high-frequency region ($10^3$–$10^6$ GHz), and their relaxation times are very short ($10^{-12}$–$10^{-16}$ s). Therefore, in most cases, electron polarization and dipole polarization are not applicable, and dipole polarization and interface polarization are the primary attenuation mechanisms of polarization loss.[69,70] Dipole polarization usually corresponds with the doping of non-metallic elements and defects. Interface polarization usually occurs at heterojunctions. Space charges accumulate at the heterojunction, forming a structure similar to a capacitor, thereby generating interface polarization and enhancing the ability to attenuate incident waves. Cole–Cole semicircles have been defined by Debye's
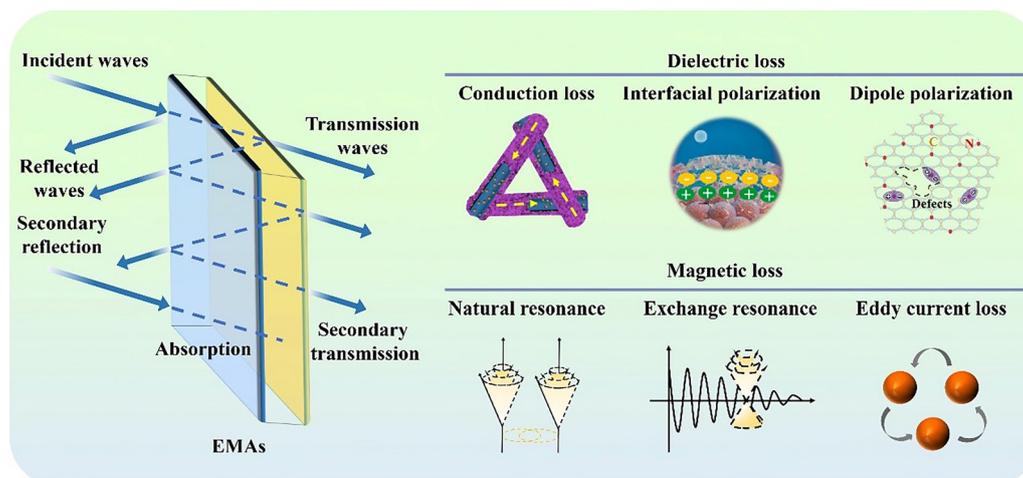


**Fig. 2** Schematic illustration of possible EMW absorption mechanisms. Reproduced with permission from ref. 85. Copyright (2023) Royal Society of Chemistry; reproduced with permission from ref. 105. Copyright (2025) Elsevier; reproduced with permission from ref. 137. Copyright (2023) Elsevier; reproduced with permission from ref. 139. Copyright (2022) Elsevier.

theory to clarify the relationship between $\varepsilon''$ and $\varepsilon'$ to characterize the relaxation process:[71,72]

$$\left(\varepsilon' - \frac{\varepsilon_s + \varepsilon_\infty}{2}\right)^2 + (\varepsilon'')^2 = \left(\frac{\varepsilon_s - \varepsilon_\infty}{2}\right)^2 \quad (7)$$

The Cole–Cole curve can be used to analyze the dielectric loss mechanisms of different samples. The Cole–Cole curve can describe the Debye relaxation process in the dielectric loss process, with each semi-circle representing a Debye relaxation process.[73]

**2.2.2. Magnetic loss.** Magnetic loss is another core attenuation mechanism of EMAs. Its essence is that under the action of alternating electromagnetic fields, the magnetic moments of materials undergo irreversible motion or the magnetic domain walls undergo irreversible displacement, converting electromagnetic energy into thermal energy.[74,75]

Generally speaking, magnetic losses include various types, such as domain wall resonance, hysteresis loss, natural resonance, and eddy current loss.[76] Domain wall resonance exists in multiferroic materials. The domain walls are forced to vibrate under weak alternating magnetic fields. When the external field frequency approaches the intrinsic vibration frequency of the domain walls, resonance occurs, resulting in energy dissipation. Domain wall resonance mainly occurs in the low-frequency range and has a relatively weak contribution in the high-frequency range, so it can be ignored.[75] Hysteresis loss is attributed to the irreversible movement of magnetic domains or the irreversible displacement of domain walls. It usually occurs under weak magnetic fields. Hysteresis loss is typically very weak and is not the main loss mechanism.[75] Natural resonance is the most significant magnetic loss mechanism in ferroelectric and other strongly anisotropic magnetic crystalline materials. Under the influence of an applied alternating magnetic field, the magnetic moment undergoes precession around its magnetic anisotropy field, and its resonance frequency satisfies the following formula:[77]

$$f_r = \frac{\gamma H_a}{2\pi} \quad (8)$$

where $f_r$ represents the resonance frequency, $H_a$ is the anisotropic field and $\gamma$ indicates the gyromagnetic ratio. When the incident EMW frequency matches $f_r$, resonance absorption occurs, and the energy is converted into lattice thermal energy *via* the intense precession of the magnetic moment.[78]

According to Faraday's law of electromagnetic induction, an alternating magnetic field will induce a closed ring-shaped current, known as eddy currents, within the conductor. When these eddies flow through materials with a certain resistivity, they generate Joule heat, thereby converting magnetic energy into thermal energy. The formula for calculating the eddy current loss coefficient ($C_0$) is as follows:[79]

$$C_0 \approx 2\pi\mu_0\mu'^2\sigma D^2 f = \mu''(\mu')^{-2}f^{-1} \quad (9)$$

If the $C_0$ remains unchanged as the frequency increases, the main source of magnetic loss may be eddy current loss.[79] However, high-frequency eddy currents generate a reverse

magnetic field, which repels the external magnetic field and penetrates deeper into the material, resulting in a decrease in magnetic conductivity.

### 2.3. EMW absorption influence factors

It is widely known that advanced EMAs can achieve good impedance matching and efficient EMW attenuation. Therefore, how to coordinate impedance matching and EMW attenuation is the core issue in practical applications. The attenuation constant ($\alpha$) can be calculated by the following formula:[80]

$$\alpha = \frac{\sqrt{2}\pi f}{c}$$
$$\times \sqrt{(\mu''\varepsilon'' - \mu'\varepsilon') + \sqrt{(\mu''\varepsilon'' - \mu'\varepsilon')^2 + (\varepsilon'\mu'' + \varepsilon''\mu')^2}} \quad (10)$$

The larger the $\alpha$ is, the faster the EMW energy is consumed, and the stronger the absorption capacity within the unit thickness of the material becomes.[81] However, various investigations have demonstrated that the performance of EMAs is not solely determined by their attenuation capacity; impedance matching, as another crucial factor, plays an indispensable part in the final absorption effect. Good impedance matching enables the incident EMWs to better penetrate into the interior of the EMAs, creating the prerequisite for subsequent attenuation and absorption of the EMWs.[82] The two must be optimized in a coordinated manner.

Dissipating reflected EMWs through the interference of EMAs is another key factor. The quarter-wavelength ($\lambda/4$) matching mechanism is described as follows:[83]

$$t_m = \frac{n\lambda}{4} = \frac{nc}{4f_m\sqrt{|\varepsilon_r\mu_r|}} \quad (n = 1, 3, 5, \ldots) \quad (11)$$

Herein $f_m$ is the matching frequency, $t_m$ is the corresponding matching thickness and $\lambda$ is the wavelength, respectively. When the $t_m$ of the material and the $f_m$ satisfy the $\lambda/4$ model, the EMWs reflected from different paths will undergo interference cancellation, thereby significantly reducing the reflection rate.[84]

## 3. Multi-scale structural design of EMAs

As we discussed above, EMAs modulated by a single chemical component struggle to satisfy the stringent requirements of high-performance EMAs. In recent years, researchers have gradually realized that the design of high-efficiency EMAs is a complex systematic form of engineering that must span multiple structural scales from the atomic to the macro level, and requires hierarchical and integrated detailed design of the EMAs. This work focuses on the design of the following four types of scale structures: (i) atomic/molecular scale, (ii) nanoscale, (iii) microscale and (iv) macroscale.

### 3.1. Atomic/molecular scale design

The atomic/molecular scale is the cornerstone of material design, determining the intrinsic electromagnetic parameters of EMAs. Design and control at this scale are crucial for the realization of ultrathin, lightweight, wideband and highly EMAs in modern technology.

**3.1.1. Atomic dispersion system.** Use of metal single atoms (M-SAs) is an emerging structural control strategy, whose core lies in precisely regulating key parameters such as the atomic arrangement on the surface, the stress state at the interface, the bridge bond configuration and the electronic structure.[86] These materials form a low-coordination environment by combining isolated metal atoms with supporting materials, allowing each atom to act as an active site, thereby achieving the maximum dispersion of metals. Unlike conventional non-metallic dopant doping, M-SAs undergo strictly atomic dispersion, with a clear coordination structure and strong metal–support interactions.[87] They have great potential in regulating the electrical conductivity and polarization of EMAs.

N-doped hollow carbon spheres (NHCS@Co-SAs) with atom-dispersed Co-SAs were designed by Li et al. using the template method (Fig. 3(a)). Multiple techniques for characterization, especially high-angle annular dark-field scanning transmission electron microscopy (HAADF-STEM) and X-ray absorption fine structure (XAFS), were employed to jointly confirm that the Co atoms existed in the carbon framework in an atomic monomer form and coordinated with four N atoms (Co–$N_4$ configuration). When the filling loading was 8 wt% and the thickness was 2 mm, NHCS@Co-SAs exhibited outstanding EMW absorption performance, with a minimum reflection loss ($RL_{min}$) of −44.96 dB and a corresponding EAB of 5.25 GHz. The introduction of Co-SAs regulated the electron structure of the carbon matrix, thereby enhancing the electrical conductivity; the Co–$N_4$ sites and the high content of pyridine N/graphite N act as polarization centers, significantly enhancing dipole and interface polarization. Density functional theory (DFT) simulations indicate that the Co–$N_4$ sites and the surrounding N doping may significantly increase the density of states near the Fermi level and cause significant charge rearrangement, resulting in a dipole moment. This, in turn, enhances both conduction loss and polarization loss simultaneously. The interaction mechanism between the HCSs and incident EMW was investigated under actual application conditions (Fig. 3(b)–(f)). By simulating the surface current density and power loss density of three samples, the reasons for the enhanced EMW absorption properties of NHCS@Co-SAs were explained. This work elucidates the dual mechanism by which M-SAs optimize impedance matching and enhance dielectric loss (conductive loss and polarization loss) by regulating the electronic structure of the carbon matrix. It also deepens understanding of the EMW absorption mechanism at the atomic scale.[88] Sun et al. have successfully constructed multi-void composite microplates (CoN$_x$C), which exhibited excellent EMW absorption performance, with a $RL_{min}$ of −63.4 dB. In the CoN$_x$C, the stable coexistence of Co nanoparticles and Co-SAs has been successfully achieved, forming rich heterogeneous interfaces and SA sites (Fig. 3(h)–(k)). The charges accumulate and rearrange at these heterogeneous interfaces, resulting in intense interface polarization, which promotes electron transport and enhances conductive loss. By controlling the N doping content, various cobalt–nitrogen coordination structures (such as CoN$_2$, CoN$_3$ and CoN$_4$) can be obtained (Fig. 3(l) and (m)). These structures break the regular charge distribution of the graphite surface, forming electric dipole moments and significantly enhancing dipole polarization. Theoretical calculations and experimental results reveal that the exceptional properties of CoN$_x$C are related to the synergistic effect of the heterogeneous interface and the SA configuration.[89] Xu et al. achieved precise anchoring of Er single atoms (Er-$N_6$) on N-doped hollow carbon nanofibers. Both theoretical and experimental results showed that the high-coordination Er-$N_6$ configuration improved conductivity and polarization loss, resulting in significantly enhanced EMW absorption performance.[90] Zhang et al. successfully dispersed Ni-SAs uniformly throughout the N-doped hierarchical porous carbon flower-like structure (Ni-SA/HPCF). This research successfully achieved the homogeneous dispersion of Ni-SAs within the carbon framework while preserving the hierarchical porous flower-like structure. The EAB reached 5 GHz, and the $RL_{min}$ was −53.2 dB. The excellent EMW absorption performance of Ni-SA/HPCF is attributed to its outstanding dielectric loss capability. Its conductivity and polarization loss are significantly higher than those of the control samples. DFT calculations indicate that the Ni–$N_4$ sites can reduce the energy band gap, increase the density of states (DOS), and enhance the conductance loss; at the same time, they cause the redistribution of charges, forming electric dipoles, and enhancing the polarization loss.[91] In practical applications under extreme conditions, the development of lightweight and acid–base resistant EMAs has attracted much attention. Lou et al. successfully synthesized N-doped porous carbon (NC) composites with hierarchical pore structures, and achieved the confined anchoring of Zn-SAs during the high-temperature carbonization process. NC-1000 exhibited outstanding EMW absorption performance and outstanding chemical stability. Its $RL_{min}$ was −50.5 dB, and the EAB was 5.1 GHz. After being immersed in strong acid and strong alkali solutions, the attenuation of its EMW absorption performance was less than 15%. The analyses confirmed that Zn exists in a monatomic form with a coordination number of 4, and the length of the Zn–N bond is approximately 2.01 Å (Fig. 3(n)–(p)). Zn-SAs can regulate the local electronic structure, providing abundant polarization sites, thereby enhancing polarization loss and electrical conduction loss.[92]

Huang et al. successfully prepared broadband EMAs with magnetic–electrostatic synergy by anchoring Zn-SAs onto the N-doped carbon shell derived from a MOF and constructing a core–shell structure (Fe$_3$O$_4$@Zn–N–carbon, FZNC) with a magnetic Fe$_3$O$_4$ core (Fig. 4(a)). Its $RL_{min}$ was −61.9 dB, and the EAB was 11.5 GHz. The dispersion states of Zn species at the atomic scale were investigated by aberration-corrected HAADF-STEM. The intensity profiles further confirmed well-dispersed atomic
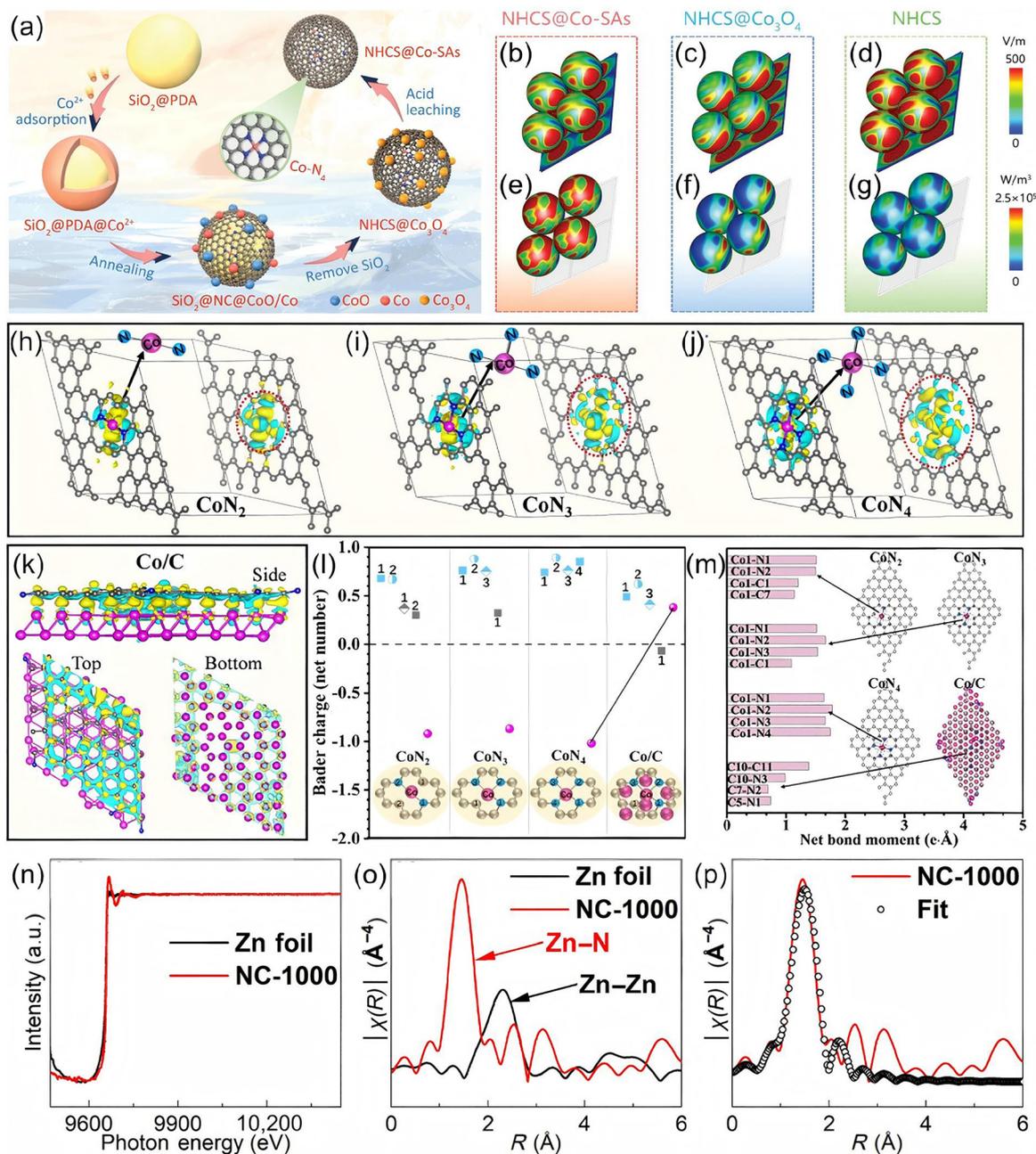

**Fig. 3** (a) Illustration of the synthesis of NHCS@Co-SAs. (b)–(d) The surface current density, and (e)–(g) the power loss density of NHCS@Co-SAs, NHCS@Co$_3$O$_4$ and NHCS. Reproduced with permission from ref. 88. Copyright (2023) John Wiley and Sons. (h)–(k) Charge density distribution on the CoN$_2$ surface, CoN$_3$ surface, CoN$_4$ surface and Co/C interface models, (l) Bader charges of the Co atom and neighboring N and C atoms in each model (gray: carbon, blue: carbon, and purple: cobalt), (m) a rough estimate of the quasi-electric dipole moment of various bonding configurations from the corresponding models. Reproduced with permission from ref. 89. Copyright (2022) Elsevier. (n) Normalized XANES spectra of NC-1000, (o) Fourier transform (FT)-EXAFS spectra of Zn foil and NC-1000, and (p) EXAFS fitting curves of NC-1000 in the $R$-space. Reproduced with permission from ref. 92. Copyright (2024) Tsinghua University Press.

Zn species in the N-doped carbon materials (Fig. 4(b)–(g)). The interface polarization is maximized by the dielectric Zn–N doped carbon layer, and the dielectric dissipation is maximized by both the interface polarization effect and the Zn-SA doping effect.[93] The SA strategy has been proven to be effective in regulating the EMW absorption performance. However, the clear correlation connection between the electronic

configuration of M-SAs and the physical loss mechanisms has not yet been established, especially at the atomic scale. Liang *et al.* synthesized Ni-SAs/N-doped carbon model (Ni-SAs*x*/NC) EMAs through a ligand polymerization strategy (Fig. 4(h)). The HAADF-TEM analysis results confirmed the existence of isolated single-Ni sites in the structure. The addition ratio of the Ni salts also affected the loading amount of Ni-SAs*x* in the
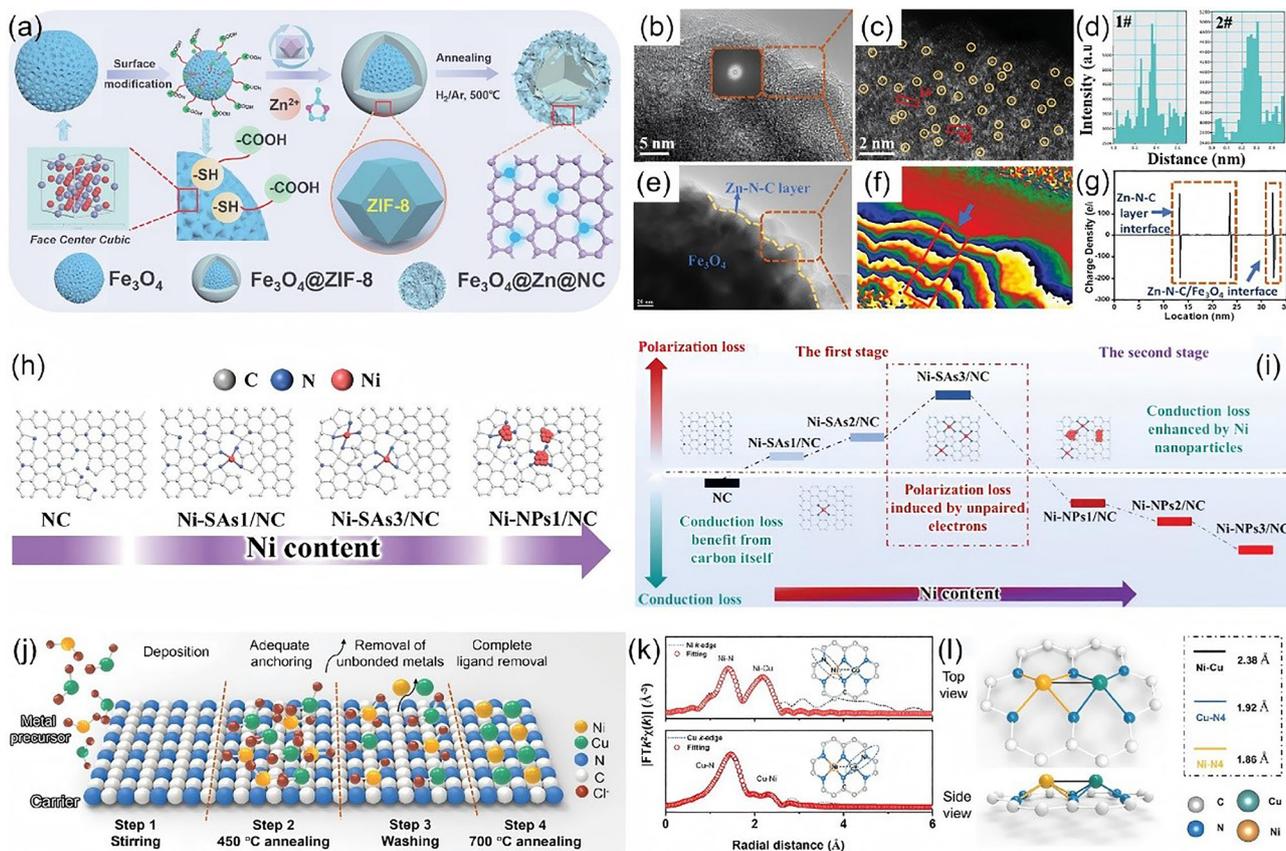
Fig. 4 (a) Schematic preparation process of $Fe_3O_4$@Zn−N−carbon composites. (e) TEM image, (b) HRTEM image, (c) enlarged HAADF-STEM image and (d) intensity profiles of FZNC-2 obtained in the dotted rectangle regions 1# and 2# in (c). (f) Reconstructed phase images from (e), and (g) the corresponding charge density distribution line profiles in the region of the green arrow for the FZNC-2 composites. Reproduced with permission from ref. 93. Copyright (2021) John Wiley and Sons. (h) Schematic illustration of the carbon trapping of metal atoms. (i) Continuous evolution mechanism of microscopic electromagnetic loss based on single-atom model absorbers. Reproduced with permission from ref. 94. Copyright (2022) John Wiley and Sons. (j) Schematic flow diagram of the stepwise process for the preparation of DA absorbers. (k) Experimental and fitting EXAFS curves for Ni/Cu-NC. (l) Structural models of Ni/Cu-NC. Reproduced with permission from ref. 96. Copyright (2024) John Wiley and Sons.

N-doped carbon materials. The individual Ni-SAs dispersed at the atomic level induce polarization loss through the unpaired electrons in the excess Ni 3d orbitals, significantly enhancing the EMW absorption performance (Fig. 4(i)). The EAB of the SA absorber (Ni-SAs3/NC) reached 7.08 GHz, covering the entire Ku band. This research proposes a novel idea for in-depth design of EMAs at the atomic scale.[94]

Metal dual atoms (M-DAs), characterized by flexible structural tunability and high atomic utilization, show significant promise for atom-level coordination engineering.[94] He *et al.* proposed an efficient strategy to enhance the EMW absorption performance of M-DA dispersed carbon-based composites, and successfully prepared EMAs (ZnCo-NC@rGO) with atom dispersion. Zn- and Co-SAs could function as effective polarization centers, effectively promoting the polarization of dipoles. The increased heterogeneous interfaces, increased point defects, and formation of capacitor-like structures induced by the bimetallic Zn/Co sites can effectively suppress excessive conductive loss and enhance magnetic loss, thereby achieving perfect impedance matching.[95] Liang *et al.* successfully fabricated a high-density Ni−Cu pair DA coupled EMAs (Ni/Cu-NC)

on a N-rich carbon substrate (NC) using a bottom-up stepwise annealing method (Fig. 4(j)). The Ni/Cu-NC achieved an EAB of 7.8 GHz and a $RL_{min}$ of −70.96 dB. The results obtained from HAADF-STEM and XAFS analysis indicate that a $N_3–Ni_1–Cu_1–N_3$ coordination spatial structure with coupled DA pairs was successfully synthesized in Ni/Cu-NC, which breaks the traditional $D_{4h}$ symmetry configuration (Fig. 4(k) and (l)). DFT calculations indicate that the cooperative effect of the Ni/Cu pairs' diatomic sites leads to the transfer of electrons from the N site to the Cu site, resulting in local charge redistribution, thereby generating strong asymmetric polarization loss and significantly enhancing the EMW absorption performance. This paper provides a theoretical basis for understanding the polarization loss mechanism at the atomic scale.[96] The above research on atomic dispersion materials has paved the way for the rational design of lightweight and high-performance EMAs at the atomic scale.

**3.1.2. Defect engineering.** Defect engineering of materials is a current research hotspot. Studies have shown defect engineering can regulate intrinsic physical properties at the atomic scale and induce valence electron migration. By

disrupting the balanced charge distribution, this approach effectively modulates polarization and conduction losses. Defect engineering of materials includes doping engineering, vacancy engineering, and lattice distortion regulation, *etc.*

Doping engineering, as an innovative strategy for optimizing material properties by regulating crystal structures and physical–chemical properties, has received extensive attention in recent years.[97] This technique, through heteroatom doping, can effectively trigger interatomic charge transfer and local charge redistribution at the atomic scale, enhance electronic interactions, and thereby significantly improve EMW absorption performance.[108] The S and P-doped graphitic carbon nitride (g-$C_3N_4$) called SP-PCN prepared by Lv *et al.* exhibited excellent electromagnetic absorption performance under high-temperature conditions. At 150 °C, the $RL_{min}$ was −50.7 dB, and the EAB was 6 GHz.[98] Tao *et al.* used the existing *in situ* N and O doping models to achieve exogenous S doping through external thermal driving. During this process, the introduced S atoms preferentially replace the pyrrole N in the material, while also causing some O atoms to be eliminated and generating O vacancies. These changes induce a dielectric polarization of 3–6 times greater than the intensity of conduction loss, and significantly improve the EMW absorption performance. The DFT analysis demonstrated the catfish effect connecting anion species and vacancy defects, proving that S doping is more likely to trigger vacancy formation. The results showed that vacancies have stronger electronic absorption capabilities, have greater influence on the charge shifts of neighboring atoms, and may even gather electrons from neighboring S regions (Fig. 5(a)–(c)). The EAB of this EMA was as high as 9.03 GHz, and the $RL_{min}$ was −64.05 dB.[99] Tian *et al.* first proposed a unique doping engineering method, using the unsaturated S doping process, to prepare S-doped $Co_xP@C$ composites with 6-coordination and 9-coordination environments. Theoretical calculations indicated that the S–C and S–$Co_6$ configurations in S–CoP@SC interact cooperatively in the 6-coordination environment, effectively improving the charge transport properties and changing the charge distribution, thereby enhancing the conductivity and polarization loss, and effectively improving the EMW absorption performance of S–CoP@SC composites (Fig. 5(d)).[100] Huang *et al.* successfully developed surface-modified NdCo composites based on N-doped carbon nanotubes (CNTs). Due to its heterostructure and doping defects, as well as the constructed robust conductive network, the N-doped CNTs significantly enhanced the dielectric loss performance. The presence of magnetic NdCo further provided magnetic loss for the attenuation of EMW.[101] Fan *et al.* successfully synthesized $Cl^-$-doped PPy nanotubes (NTs) *via* a soft template-assisted oxidation method (Fig. 5(e)). Theoretical results indicated that the band structure of PPy could be adjusted and its conductivity enhanced by modulating the $Cl^-$ doping level. There are many lattice defects in $Cl^-$-doped PPy nanotubes (PPy-M-4), which act as dipole centers, enhancing dipole/defect polarization and improving EMW absorption performance (Fig. 5(f)). PPy-M-4 exhibits excellent EMW absorption (3.32 GHz $mm^{-1}$) and radar cross section (RCS) reduction

performance (33.45 dB $m^2$). Furthermore, by precisely controlling the $Cl^-$ doping level and nanotube structure, $Cl^-$-doped PPy NT/silicone membranes show high thermal conductivity (3.597 W $m^{-1}$ $K^{-1}$) (Fig. 5(g)).[102] Wang *et al.* successfully fabricated mesoporous N-doped mesoporous hollow nanospheres (HNSs) by using a template-assisted carbonization-etching process combined with the N doping strategy. The prepared N-doped mesoporous HNSs exhibit advanced EMW absorption performance and good corrosion resistance. The intrinsic defects and functional group defects of amorphous carbon, combined with those generated by N doping, collectively form a large number of dipoles, which leads to strong dipole polarization and enhanced EMW dissipation performance (Fig. 5(h)).[103] Lu *et al.* successfully prepared nitrogen-doped biomass-derived carbon (NBC) with a porous structure through a two-step process of hydrothermal treatment and carbonization. The excellent EMW absorption capacity of this material stems from its abundant N doping and porous structure. The N-doped atoms and defect structures can promote dipole polarization under alternating electromagnetic fields.[104] Guan *et al.* successfully prepared N-doped reduced graphene oxide/zinc ferrite@polypyrrole (NRGO/$ZnFe_2O_4$@PPy) composite aerogels through a three-step process of solvothermal, *in situ* polymerization and hydrothermal method. This N-doped composite achieved a $RL_{min}$ of −77.8 dB and the minimum RCS value reached −47.9 dB $m^2$. Furthermore, successfully introducing N atoms into the graphene lattice would disturb the originally complete $sp^2$ hybridization structure of C atoms, resulting in an enormous number of disordered sites. Due to the substantial difference in electronegativity between C and N elements, numerous C–N electric dipoles can be formed, dissipating electromagnetic energy *via* the dipole polarization effect.[105] He *et al.* prepared ordered mesoporous M-type barium ferrite (M-BaM) by using sodium dodecyl sulfate (SLS) and cetyltrimethylammonium bromide (CTAB) as dual templating agents through the sol–gel method. Subsequently, M-BaM was combined with GO through the hydrothermal method, simultaneously achieving the reduction and N doping of GO, forming the M-BaM/N-RGO composites. The surface of N-RGO contains a large number of oxygen-containing functional groups, intrinsic defects, and N-doped defects, which are conducive to defect polarization and dipole polarization relaxation (Fig. 5(i)). The $RL_{min}$ of the composites arrived at −62.6 dB, and the EAB was extended to 4.2 GHz.[106]

Vacancy engineering provides a key strategy for optimizing material properties. By controlling the formation, type, and concentration of vacancies, it is possible to precisely modulate the electronic structure of materials, enhance the interaction between electrons, and improve charge transfer efficiency.[109] Zhao *et al.* successfully prepared a unique nested doll structure of $MoS_2/V_2O_3$ composites. By regulating the concentration of $S^{2-}$, the lattice spacing and interface vacancies of molybdenum disulfide nanosheets can be simultaneously adjusted. A higher concentration of $S^{2-}$ will cause the lattice spacing of molybdenum disulfide to expand and the interface vacancies to increase, thereby precisely controlling the ordered stacking
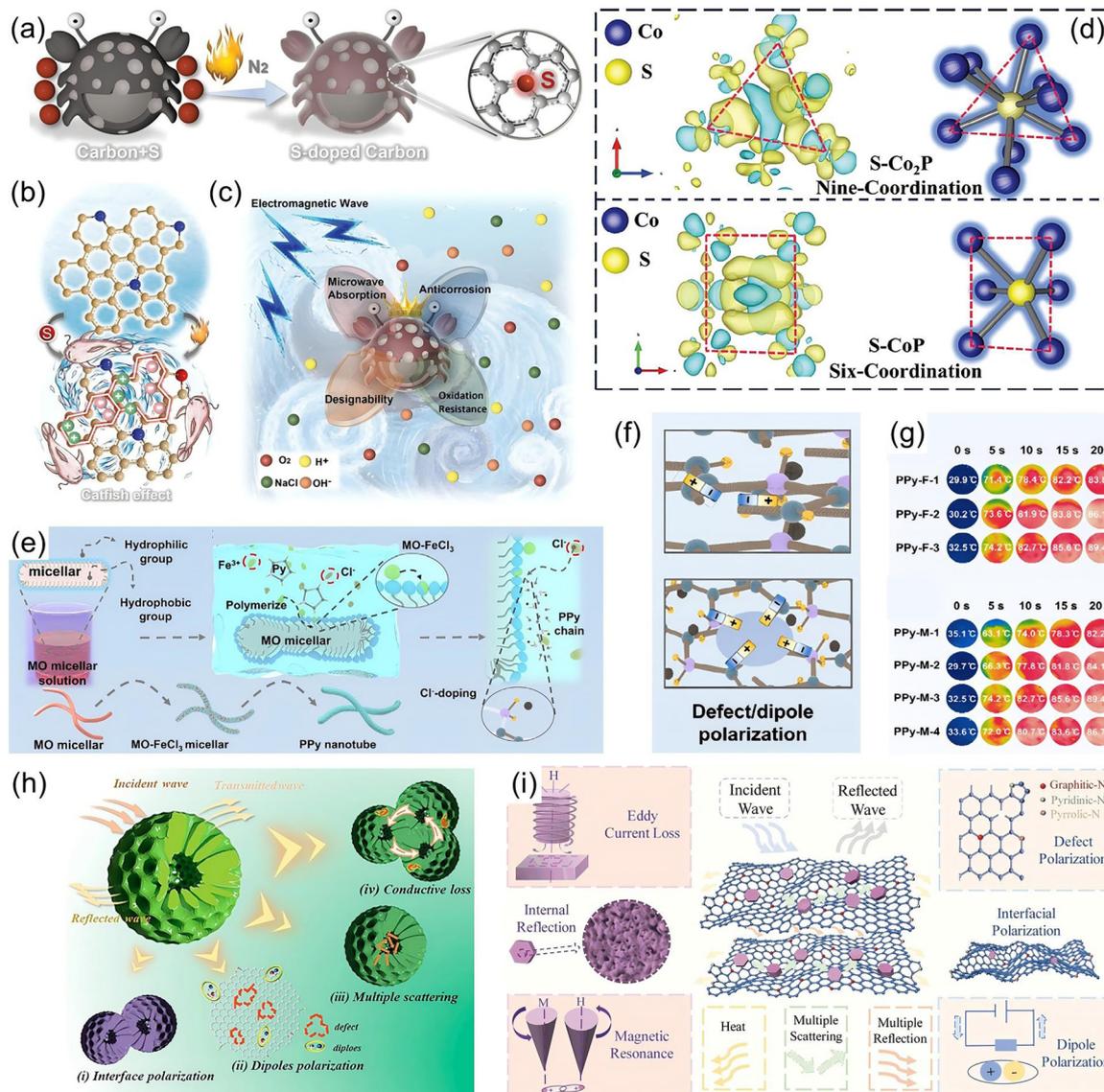
**Fig. 5** (a) Preparation route of S-doped porous carbon micro-flakes. (b) Schematic diagram of the catfish effect. (c) Comprehensive ability index of crab-derived absorbers. Reproduced with permission from ref. 99. Copyright (2022) John Wiley and Sons. (d) Diagram of 9 and 6-coordination configurations and differential charges. Reproduced with permission from ref. 100. Copyright (2023) John Wiley and Sons. (e) Growth mechanism of $Cl^-$-doped PPy NTs. (f) Defect/dipole polarization. (g) Infrared images. Reproduced with permission from ref. 102. Copyright (2025) John Wiley and Sons. (h) EMW absorption mechanism of N-doped mesoporous HNSs. Reproduced with permission from ref. 103. Copyright (2026) Elsevier. (i) Schematic diagram of the EMW absorption mechanisms for the composites. Reproduced with permission from ref. 106. Copyright (2023) John Wiley and Sons.

structure of the $MoS_2$–$V_2O_3$–$MoS_2$ layers and inducing an interface polarization effect (Fig. 6(a)). The introduction of vacancies effectively reduces the band gap of molybdenum disulfide, lowers the energy barrier for electron transition, and simultaneously enhances the dielectric loss capacity (Fig. 6(b) and (b1)). These changes contribute greatly to the material's EMW absorption capability.[107] Jia *et al.* successfully achieved local charge regulation in dielectric $CoSe_2$ through Se vacancy engineering, thereby enhancing the EMW absorption ability. The experimental results demonstrated that the concentration of Se vacancies may be efficiently regulated by controlling the re-annealing temperature. The formation of Se vacancies

significantly improves the conductivity of $CoSe_2$, thereby enhancing the material's conductive loss capacity. Moreover, the DFT calculations further reveal that the Se vacancies disrupt the original charge balance distribution in $CoSe_2$, inducing a strong dipole polarization effect, which further promotes the polarization loss.[108] Gong *et al.* were the first to propose the introduction of Se vacancies at the heterogeneous interface formed by Fe–Se compounds (Fig. 6(c)). It is noteworthy that the formation of Se vacancies significantly promotes the electron transfer from Fe atoms to Se atoms, thereby generating a large number of dipoles and enhancing the polarization loss ability of the material. In addition, the Se vacancies can act as
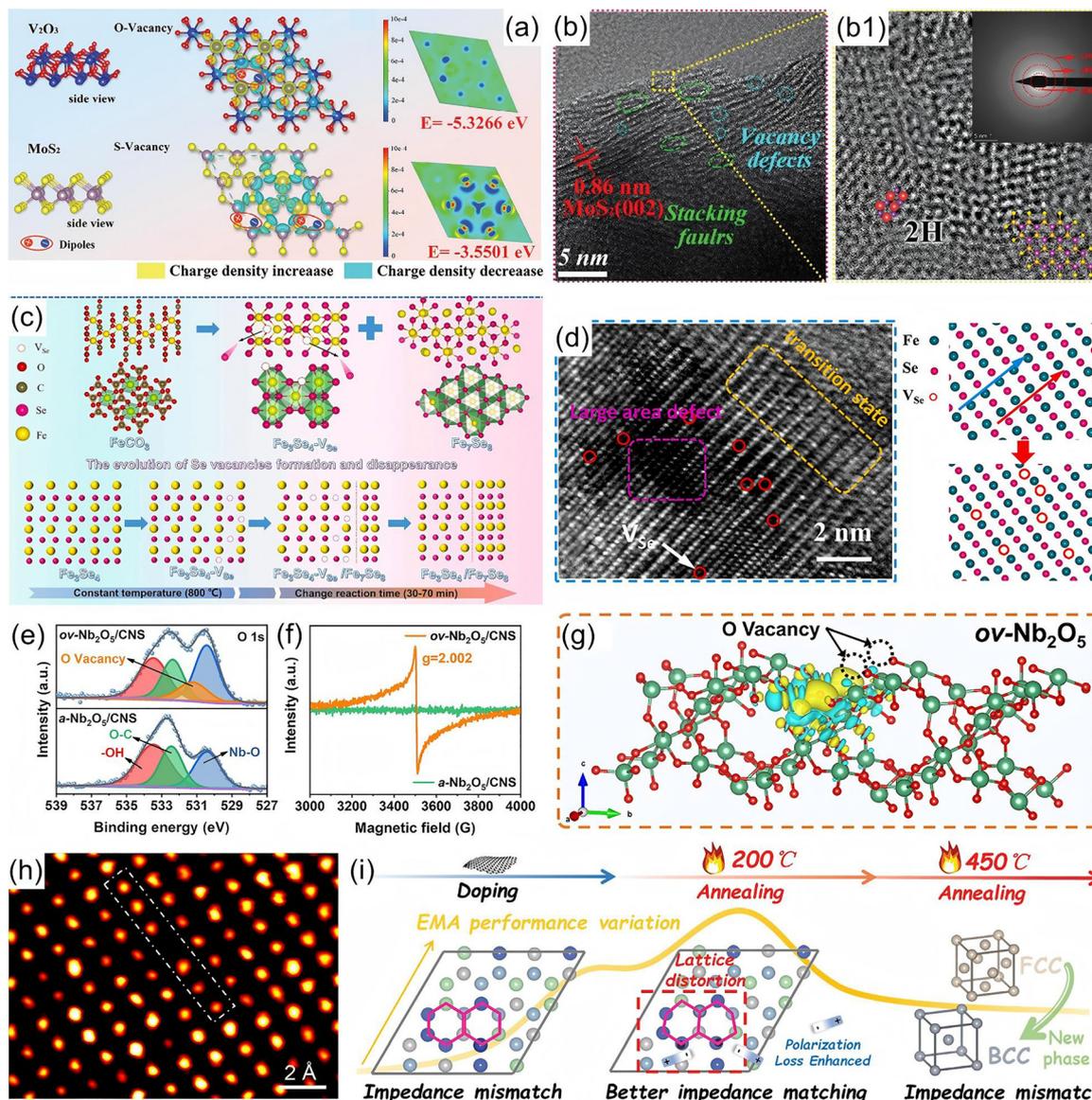
Fig. 6 (a) Differential charge 3D plots and 2D cut-away plots of O-vacancy $V_2O_3$ and S-vacancy $MoS_2$. (b) and (b1) HR-TEM images of the $MoS_2/V_2O_3$-5 absorber. Reproduced with permission from ref. 107. Copyright (2024) John Wiley and Sons. (c) Evolution diagram of the Se vacancies. (d) Enlarged HR-TEM image. Reproduced with permission from ref. 109. Copyright (2023) Elsevier. (e) High-resolution O 1s XPS spectra and (f) EPR spectra of $a$-$Nb_2O_5$/ CNS and $ov$-$Nb_2O_5$/CNS. (g) Charge density distribution of $ov$-$Nb_2O_5$ (yellow and blue regions depict aggregation and dispersion of electrons). Reproduced with permission from ref. 111. Copyright (2023) Springer Nature. (h) Atomic-resolution HAADF-STEM image of the 8HEB (8-cation HEB) samples. Reproduced with permission from ref. 113. Copyright (2025) Elsevier. (i) Schematic diagram of induced lattice distortion to enhance impedance matching and electromagnetic loss mechanism to achieve the regulation of $FeCoNiCuC_x$ absorption performance. Reproduced with permission from ref. 114. Copyright (2024) John Wiley and Sons.

binding centers, capturing free electrons around them, and reducing the overall conductivity of the material (Fig. 6(d)). This behavior not only weakens the skin effect but also helps to optimize the impedance matching characteristics. By precisely controlling the Se vacancies in the Fe–Se compound, excellent EMW absorption performance was successfully achieved at an ultrathin thickness. The EAB at 1.5 mm was 5.42 GHz.[109] Hao *et al.* successfully achieved efficient EMW absorption by constructing abundant oxygen vacancies in $Co_3O_4$/C/N-doped carbon nanonets (NCNs). The introduction of oxygen-rich

vacancies enhanced the polarization effect and conductivity, resulting in a $RL_{min}$ of −78.1 dB.[110] Su *et al.* successfully integrated ultrafine vacancy-rich $Nb_2O_5$ semiconductors into carbon nanosheets. The O 1s XPS spectra revealed the existence of O vacancies in $Nb_2O_5$, and EPR analysis also verified the existence of O vacancy defect sites (Fig. 6(e) and (f)). When there are two oxygen vacancies, electrons will delocalize at the vacancies and flow into the nearby O atoms, thereby causing the separation of charges, generating electric dipoles, and forming electron dipole polarization, significantly increasing

the dielectric loss ability of the material (Fig. 6(g)).[111] Zhang et al. successfully developed a highly efficient EMA composed of one-dimensional carbon fibers and cation-doped NiCo-MOF (CF@NiCoMOF-800). By adjusting the O vacancies distribution of the NiCo-MOF through different radii of cation atoms, the resulting EMAs exhibited excellent EMW absorption performance, with a $RL_{min}$ of −80.63 dB and an EAB of up to 8.01 GHz.[112]

Lattice distortion refers to the deviation of the periodic arrangement of atoms in a crystal from their ideal positions, resulting in structural defects, stress or distortion. This change in structure significantly affects the electronic structure and electromagnetic parameters of the absorber, and the electromagnetic parameters directly determine the material's EMW absorption performance. Gu et al. successfully prepared high-entropy diborides (HEB) through lattice distortion engineering. By adjusting the composition of the metal elements, they rationally designed the lattice distortion structure of the HEB, achieving superior EMW absorption performance with an EAB of 7.2 GHz (Fig. 6(h)).[113] Qiu et al. precisely controlled the lattice distortion of the FeCoNiCu high entropy alloys through doping and annealing processes, successfully observing significant lattice distortion in the composites (Fig. 6(i)). The EAB of the composites was 7.99 GHz. Its outstanding EMW absorption capability was attributed to the optimized impedance matching and enhanced polarization loss[114] (Table 1).

## 3.2. Nanoscale design

Rational nanoscale design is one of the key strategies for constructing lightweight and efficient EMAs. Through nanoscale design, unique physical and chemical properties can be endowed to EMAs, such as size effect, large specific surface area, multiple loss synergies and precisely controllable microstructures.

**3.2.1. Regulation of nanostructure morphology.** In recent years, researchers have developed various nanostructured morphologies to enhance the EMW absorption performance, including hollow structure, porous structure, and core–shell structure.[40] Obviously, compared with traditional EMAs, these structures not only have significant advantages such as being lightweight, but are also convenient for creating composites with other functional materials owing to their huge specific surface area.

The hollow structure, with its abundant cavities, can effectively regulate the conductive properties, promote multiple reflections and scattering, and improve impedance matching, thereby considerably improving the EMW absorption capacity.[117,118] Xu et al. successfully prepared silicon oxycarbonitride (SiOCN) ceramics with a hollow bowl-like morphology via a template-free pyrolysis strategy (Fig. 7(a)–(d)). The resulting material exhibited excellent EMW absorption performance, achieving a $RL_{min}$ of −52.93 dB and an EAB of 3.88 GHz. Besides, the RCS decreased by more than 15 dB m². This enhanced attenuation performance was attributed to the unique hollow architecture, which facilitates multiple scattering events and optimizes impedance matching.[115] Zhang et al.

**Table 1** EMW absorption performance of atomic/molecular scale structure absorbers

| Absorbers | $RL_{min}$ (dB) | EAB (GHz) | Thickness (mm) | Ref. |
|---|---|---|---|---|
| NHCS@Co-SAs | −44.96 | 5.25 | 2 | 88 |
| $CoN_{20}C$ | −63.4 | — | 2.78 | 89 |
| HCNF-Er-based film | −57.8 | 6 | — | 90 |
| Ni-SA/HPCF | −53.2 | 5 | — | 91 |
| NC-1000 | −50.5 | 5.1 | 1.9 | 92 |
| $Fe_3O_4$@Zn–N–carbon | −61.9 | 11.5 | 2.5 | 93 |
| Ni-SAs3/NC | — | 7.08 | 2.5 | 94 |
| ZnCo-NC@rGO | −59.63 | 4.52 | — | 95 |
| Ni/Cu-NC | −70.96 | 7.8 | — | 96 |
| SP-PCN | −50.7 | 6 | 1.8 | 98 |
| S3PC | −64.05 | 9.03 | — | 99 |
| S-CoP@SC | −66 | 5 | 2.2 | 100 |
| NdCo@C/CNTs-2 | −66.31 | 4.74 | 1.34 | 101 |
| PPy-M-4 | — | 6.64 | 2 | 102 |
| HNSs | −51.39 | 7 | 1.96 | 103 |
| NBC | −53 | 4.22 | 1.7 | 104 |
| NRGO/$ZnFe_2O_4$@PPy | −77.8 | 6.4 | — | 105 |
| MBG-2 | −62.6 | 4.2 | 1.4 | 106 |
| $MoS_2/V_2O_3$-5 | −69.65 | 7.68 | 3 | 107 |
| $CoSe_2$-600 | −30.73 | 4 | 1.8 | 108 |
| $Fe_3Se_4/Fe_7Se_8$ | −42.4 | 5.42 | — | 109 |
| NCM-350 | −78.1 | 6.83 | — | 110 |
| ov-$Nb_2O_5$/CNS | −80.8 | — | 2.76 | 111 |
| CF@NiCoMOF-800 | −80.63 | 8.01 | 2.59 | 112 |
| 9HEB | −42.6 | 7.2 | — | 113 |
| $FeCoNiCuC_{0.37}$ | — | 7.99 | 1.95 | 114 |

successfully synthesized a Co–$CoFe_2O_4$@mesoporous hollow carbon sphere (PCHMs) nanocomposite using a hard template and subsequent pyrolysis process. Owing to the unique hollow structure of the Co–$CoFe_2O_4$@PCHMs, via adjusting the content of Co–$CoFe_2O_4$ nanoparticles, the electromagnetic parameters of the composites could be flexibly regulated, effectively controlling the EMW absorption performance of the Co–$CoFe_2O_4$@PCHMs. When 0.1 mmol $Co(NO_3)_2$·$6H_2O$ and 0.2 mmol $Fe(NO_3)_3$·$6H_2O$ were added, the $RL_{min}$ of Co–$CoFe_2O_4$@PCHMs reached −65.31 dB, and the EAB was 8.48 GHz.[116] Xiao et al. successfully fabricated a kind of hollow silicon carbide (SiC) microtubes with a special structure through the de-templating method (Fig. 7(e) and (f)). The carbon element was evenly distributed within the hollow SiC microtubes, which helps to improve the conductive loss of the composites. Furthermore, the SiC microtubes' unique hollow structure facilitated multiple EMW reflections and scattering. For the SiC-T2 sample, prepared with an initial Si/C molar ratio of 0.2:1, the $RL_{min}$ reached −25.7 dB and the EAB was 5 GHz.[117] Qiu et al. successfully synthesized a nickel metal–organic framework (Ni-MOF) using a mixed solvent through the solvothermal method, and then obtained hollow nickel/carbon (Ni/C) microspheres by pyrolysis of Ni-MOF. This study found that by adjusting the ratio of N,N-dimethylformamide (DMF) and $H_2O$ in the solvent, the morphology of Ni-MOF could be effectively controlled. When the ratio of DMF to $H_2O$ in the solvent was 2:1, the $RL_{min}$ of the hollow Ni/C-20 composites was −57.25 dB, and the EAB was 5.1 GHz. The unique hollow structure and the synergistic effect between C nanoparticles and Ni nanoparticles all led to the excellent EMW absorption capability.[118] Sun et al. successfully coated $MoS_2$ on
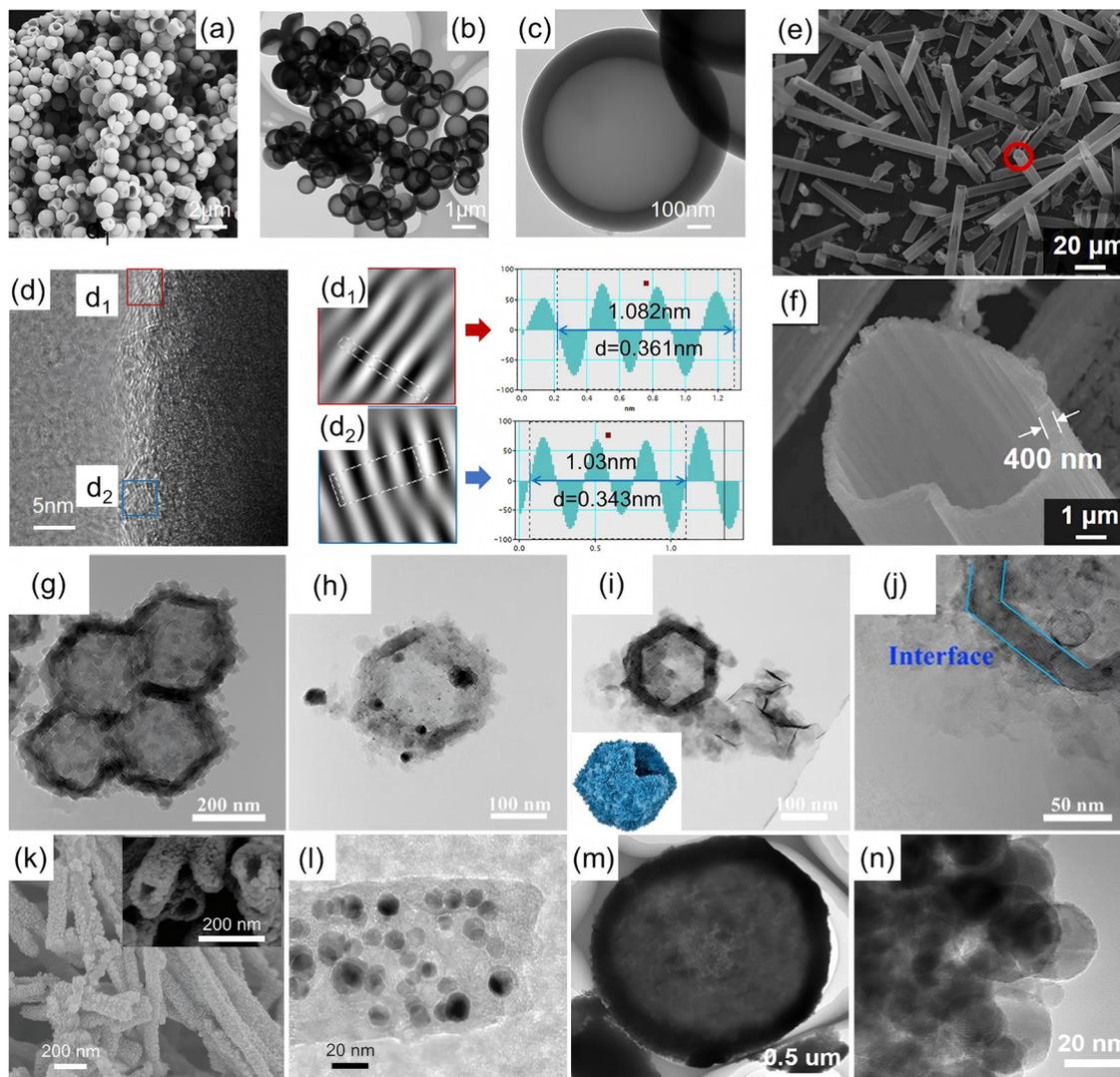
**Fig. 7** (a) SEM, (b) and (c) TEM, and (d) HRTEM, IFFT images and line profiles of the hollow SiOCN bowl. Reproduced with permission from ref. 115. Copyright (2024) Royal Society of Chemistry. (e) The SEM and (f) magnification images of SiC-T2. Reproduced with permission from ref. 117. Copyright (2020) Elsevier. TEM images of (g) ZIF-67-TA, (h) HCN700, and (i) HCNS700. (j) Partial enlarged view of (i). Reproduced with permission from ref. 119. Copyright (2025) American Chemical Society. (k) SEM and (l) TEM images of 1.2Ni-HMCNTs-800. Reproduced with permission from ref. 121. Copyright (2024) John Wiley and Sons. (m) and (n) TEM images of Ni/Ni$_2$P/CNs-2. Reproduced with permission from ref. 122. Copyright (2023) Royal Society of Chemistry.

a MOF-derived hollow MoS$_2$@CNS@CoS$_2$ composite (HCNSs) through tannic acid-protected etching, carbonization and hydrothermal techniques (Fig. 7(g)–(j)). The special hollow structure of HCNSs brought excellent performance to the material. When the carbonization temperature was 700 °C, the HCNS700 exhibited a RL$_{min}$ of −63.63 dB and the EAB extended to 6.69 GHz. In addition, HCNS700 also has excellent radar stealth performance.[119] Liu *et al.* used hollow carbon microcapsules (HC) as the core and synthesized several mutually intersecting nanosheets of MoS$_2$ on the surface of the HC (HCM). The hollow structure with strong dielectric loss capability could promote multiple reflections of incident waves. Additionally, the construction of the MoS$_2$ shell layer increased the heterogeneous interfaces and enhanced interface

polarization. The EAB was 6.1 GHz.[120] Chen *et al.* successfully prepared 1D magnetic nickel–carbon matrix nanotube composites (nNi-HMCNTs-800, where *n* represents the mmol amount of Ni(NO$_3$)$_2$·6H$_2$O, and 800 refers to the calcination temperature) by mixing hydrogen bond organic frameworks (HOFs) and MOFs (Fig. 7(k) and (l)). This synthesis involved a transformation from HOF-to-MOF, characterized by the penetration of Ni ions into the HOF structure *via* a competitive coordination reaction, thereby forming the hollow structure of Ni-HMNTs. The air/CNT in the hollow structure play an effective role in regulating impedance matching. The RL$_{min}$ of the 1.2Ni-HMCNTs-800 composites was −56.9 dB, and the corresponding EAB was 5.95 GHz.[121] Wang *et al.* proposed an internal-to-external Ostwald ripening and phase evolution technique,

successfully synthesizing uniform-sized hollow N-doped carbon spheres with Ni/Ni$_2$P heterojunctions (Ni/Ni$_2$P/CNs). When the addition amount of NaH$_2$PO$_2$ was 1000 mg, Ni/Ni$_2$P/CNs-2 exhibited outstanding EMW absorption performance, with a RL$_{min}$ of −72.2 dB and the corresponding EAB was 5.8 GHz. The experimental results and simulation analysis indicated that the large-sized internal cavities of Ni/Ni$_2$P/CNs-2 microspheres played a crucial role in the EMW absorption performance (Fig. 7(m) and (n)).[122]

The porous structure can not only improve the impedance matching of EMAs, increase the efficiency of EMW penetration through the materials, and extend the propagation path, but can also improve the interface polarization effect.[123] Shi et al. successfully prepared porous FeNi powder by using the spray pyrolysis reduction method and adjusting the concentration of

nitrate (Fig. 8(a)). The porous structure provided abundant heterogeneous interfaces, enhancing the interface effect and promoting further dissipation of EMW energy. The RL$_{min}$ of the FeNi powder was −60.2 dB, and a general EAB reached 3.38 GHz.[123] Lv et al. reported a method for synthesizing graphene using a nanoparticle template with monodisperse and staggered circular nanopores. This structure realizes the electromagnetic-heat-direct current conversion pathway (Fig. 8(b)). Through experiments and theoretical analysis, it was confirmed that this staggered nanoporous structure alters the electronic and phonon properties of graphene by co-coordinately regulating the nanoscale structures within the layers and the interlayer interactions.[124] Li et al. successfully prepared homogenous Co/nanoporous carbon (NPC) nano-islands via effective co-precipitation along with in situ pyrolysis
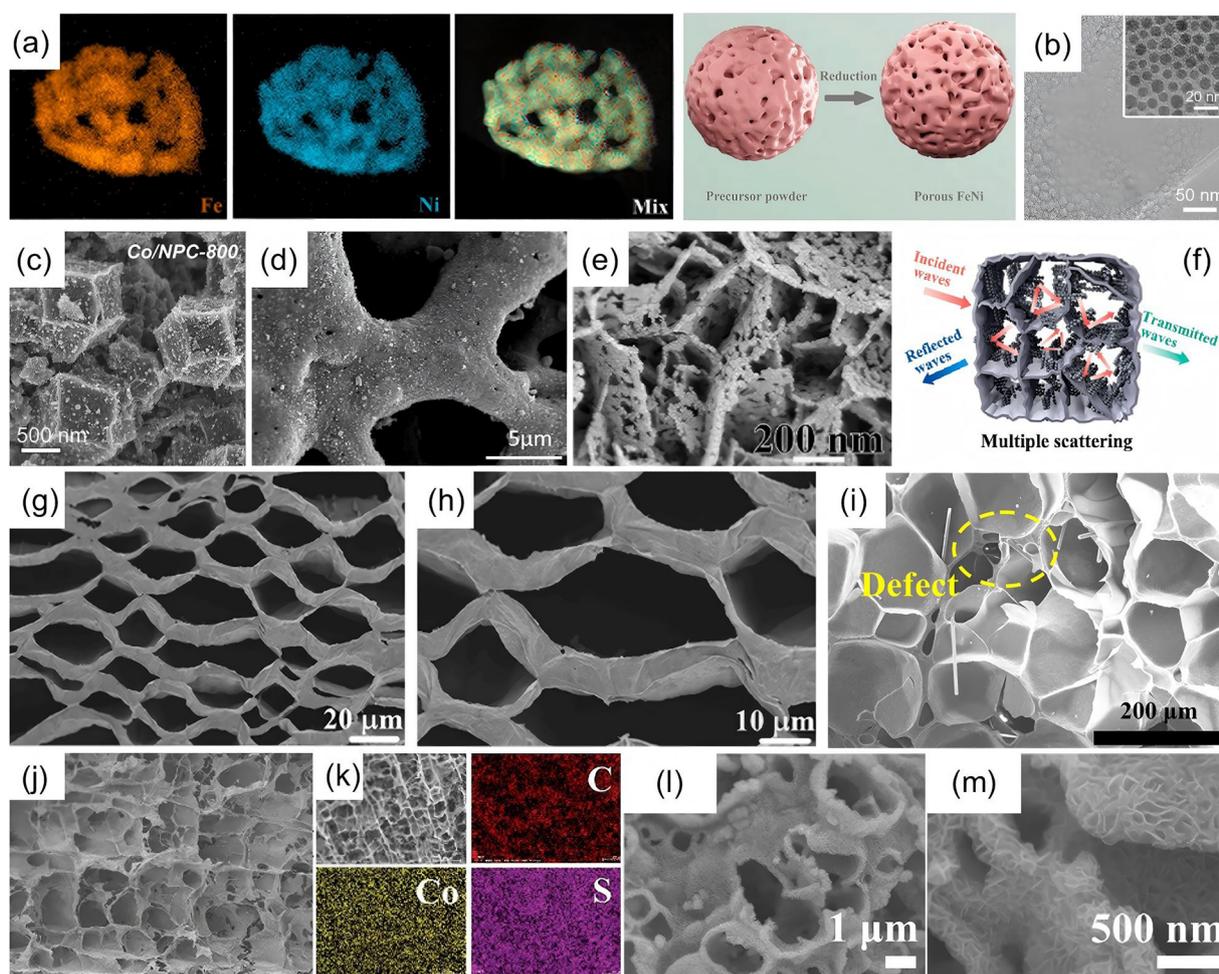


Fig. 8 (a) TEM images of porous FeNi powders prepared with 1.50 mol L$^{-1}$ KNO$_3$. Reproduced with permission from ref. 123. Copyright (2025) Elsevier. (b) TEM image of monolayer graphene with circular pores with a diameter of 6 ± 1 nm. Reproduced with permission from ref. 124. Copyright (2023) Springer Nature. (c) SEM image of Co/NPC-800. Reproduced with permission from ref. 125. Copyright (2023) John Wiley and Sons. (d) SEM image of ZnOCo@C-2. Reproduced with permission from ref. 127. Copyright (2023) Elsevier. (e) SEM image of GMF. (f) Part of the EMW absorption mechanisms in GMF foam. Reproduced with permission from ref. 128. Copyright (2023) Elsevier. SEM images of the MOPCN samples: (g) and (h) top view of the MOPCN-x/y-A specimen with a honeycomb pattern. Reproduced with permission from ref. 130. Copyright (2023) Elsevier. (i) SEM image of CP-3. Reproduced with permission from ref. 131. Copyright (2022) Springer Nature. (j) SEM image of CSC-70 and (k) EDS mapping of CSC-70 with the elements C, S and Co. Reproduced with permission from ref. 132. Copyright (2024) John Wiley and Sons. (l) and (m) SEM images of MS/MC/PNC-2. Reproduced with permission from ref. 133. Copyright (2024) Tsinghua University Press.

(Fig. 8(c)). By adjusting the pyrolysis temperature, they achieved effective control over the EMW absorption capacity. At 800 °C heating temperature, Co/NPC-800 exhibited excellent EMW absorption performance, with a RL$_{min}$ of −73.87 dB and a broad EAB extended to 6.64 GHz. The porous nanostructure of Co/NPC-800 not only enhanced multiple reflections but also improved the interface polarization effect.[125] Liu *et al.* prepared a MOF derived Fe/Fe$_3$Co$_7$/Co/C composite with high porosity. They systematically studied the impedance and attenuation characteristics of single-pore and gradient-pore derivatives. At a thickness of 2.5 mm, the RL$_{min}$ of the Fe/Fe$_3$Co$_7$/Co/C composites reached −64.7 dB, and the EAB was as wide as 5.8 GHz.[126] Wang *et al.* successfully constructed a three-dimensional ZnOCo@C material with a sub-millimeter porous structure and rich heterogeneous interfaces by introducing Co elements for co-coordination during the preparation of Zn-based MOFs, followed by pyrolysis. The sub-millimeter-sized pore structure can effectively absorb EMW (Fig. 8(d)). The composites prepared with a Zn:Co ratio of 5:1 was labeled as ZnOCo@C-3. ZnOCo@C-3 exhibited a wide EAB of 6.12 GHz and a RL$_{min}$ of −46.77 dB.[127] Li *et al.* constructed a porous graphene magnetic composite foam (GMF) loaded with Fe$_2$O$_3$ (Fig. 8(e)). Thanks to the construction of micro-to nano-sized pores, the incident EMW could undergo multiple scattering and dissipate as fully as possible after entering the foam (Fig. 8(f)). The GMF had a RL$_{min}$ of −60.13 dB and a EAB extended to 6.23 GHz.[128] Lv *et al.* constructed a unique two-dimensional graphene superlattice by stacking graphene sublattices with monodisperse, nanometer-sized, square-shaped pores and strategically doped elements at the pore edges. The resulting graphene superlattice exhibited significant quantum phase correlations at both the electronic and phononic levels, thereby enabling various functions such as energy harvesting, optoelectronics, and thermoelectric effects.[129] Tian *et al.* successfully prepared the macro-ordered porous carbon nanocomposites composed of MWCNTs and CHI (MOPCN-*x*/*y*, where *x*/*y* donates the corresponding mass ratio of multi-walled carbon nanotubes (MWCNTs) to chitosan (CHI) in the precursor solution) by using the freeze casting technique. By adjusting the freezing temperature gradient, they prepared an axial (A) honeycomb-like pore array (Fig. 8(g) and (h)). The findings from the experiments revealed that the RL$_{min}$ of the MOPCN-1/2-A composites reached −72.9 dB.[130] Jiao *et al.* developed a porous carbon fiber/polyacrylamide (CP) composite frame that simultaneously exhibited high temperature resistance and high strength (Fig. 8(i)). The sample with a mass fraction of CF in monomer of 3% (CP-3) exhibited an ultra-high EAB of 14.1 GHz at room temperature and could also cover the X-band at 473 K. The superior EMW absorption performance was due to the porous structure of the composites, which could optimize impedance matching and achieve multiple reflections.[131] Su *et al.* precisely constructed the structure and defects through controlled migration of S atoms, and conducted experimental verification based on the Kirkendall effect and heterogeneous atomic S doping. The study showed that low-concentration sulfur vapors mainly formed a hollow structure, while excessive

vapors will simultaneously produce both a hollow structure and point defects (Fig. 8(j) and (k)). When the amount of sulfur powder added was 70 mg, the RL$_{min}$ of the cobalt sulfide/S-doped carbon (CSC-70) aerogel was −52.82 dB, and it achieved a broad EAB of 8.82 GHz. In addition, the aerogels also possessed superhydrophobic properties and excellent thermal insulation performance.[132] Zhao *et al.* designed molybdenum disulfide-modified/molybdenum carbide/porous nitrogen-doped carbon (MS/MC/PNC) composites with a three-dimensional porous structure through the salt melt synthesis (SMS) method (Fig. 8(l) and (m)). By changing the mass ratio of molybdenum/sulfur sources in the composites, the EMW absorption capability of the MS/MC/PNC composites could be effectively controlled. When the mass ratio of molybdenum/sulfur sources was 0.52 g/0.9 g, the RL$_{min}$ of MS/MC/PNC-2 was −55.3 dB, and the EAB was 7.6 GHz.[133]

The core–shell structure design is one of the most common design strategies in nanoscale design. This structure can usually protect the core layer from external interference, and the core and shell layers can also work in synergy to attenuate incident waves. Furthermore, by adjusting the material kind, thickness, and morphology of the shell and core layers, multiple loss mechanisms can be achieved, dielectric properties can be modulated, and impedance matching can be optimized.[134,135] Shi *et al.* successfully prepared novel core–shell structured Fe$_3$O$_4$@C microspheres through polydopamine (PDA) confined pyrolysis (Fig. 9(a)). The core–shell design endowed the Fe$_3$O$_4$@C microspheres with strong magnetic and dielectric losses, and formed abundant heterogeneous interfaces, enhancing the interfacial effect. The RL$_{min}$ of the Fe$_3$O$_4$@C microspheres reached −55.4 dB, with an EAB as high as 9.5 GHz (8.5–18 GHz).[134] Wang *et al.* coated a layer of PDA onto the outside of a FeCo Prussian blue analog (FeCo PBAs), and then under an argon atmosphere, core–shell FeCo@C nanoparticles encased within carbon nanocages derived from PDA (FeCo@C@CNGs) were obtained *via* pyrolysis at 600 °C for 2 h (Fig. 9(b)). By adjusting the proportion of DA to the FeCo PBAs, the EMW absorption capacity could be effectively improved. When the mass proportion of DA to FeCo PBAs approached 0.75, the RL$_{min}$ of FeCo@C@CNGs-0.75 was −67.8 dB, and the EAB was 5.3 GHz.[135] To address the imbalance of impedance issue owing to the high electrical conductivity of Ti$_3$C$_2$T$_x$ MXene, Jiang *et al.* successfully fabricated SiO$_2$@MXene@MoS$_2$ nanospheres with a core–shell structure by combining electrostatic self-assembly with hydrothermal processing (Fig. 9(c)). The core–shell structure prevented the aggregation of MXene and MoS$_2$. The presence of SiO$_2$ enabled the SiO$_2$@MXene@MoS$_2$ nanospheres to have an appropriate dielectric constant, effectively regulating the impedance matching (Fig. 9(d) and (e)). The RL$_{min}$ of the SiO$_2$@MXene@MoS$_2$-2 (sample with amounts of 0.484 g Na$_2$MoO$_4$·2H$_2$O and 0.608 g C$_2$H$_5$NS) was −52.11 dB, and the corresponding EAB was 5.44 GHz.[136] By employing *in situ* polymerization of pyrrole combined with hydrazine vapor reduction, Dong *et al.* successfully synthesized reduced graphene oxide (rGO) nanosheets decorated with core–shell Fe$_3$O$_4$@polypyrrole (FP)
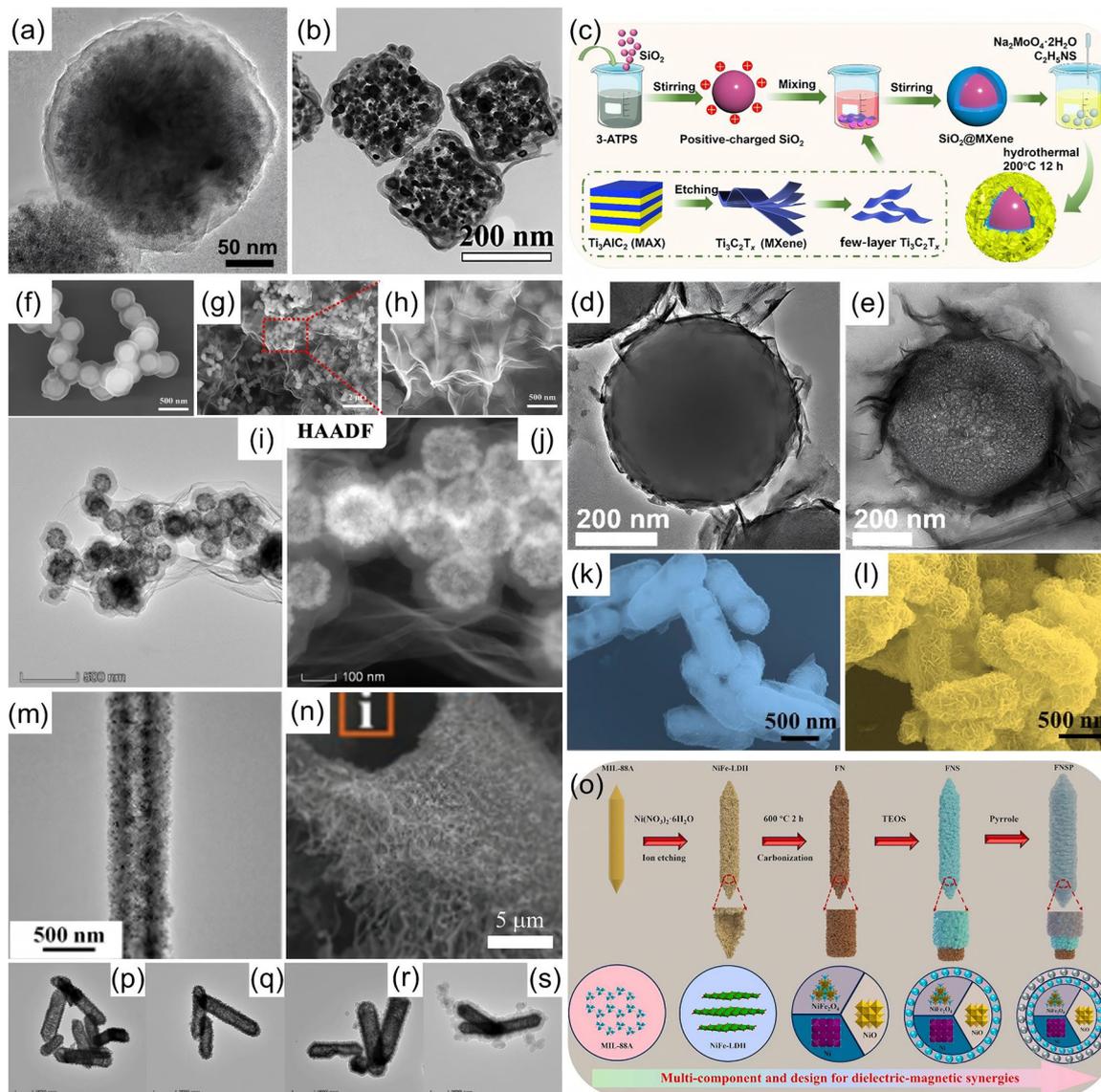
**Fig. 9** (a) TEM image of the core–shell $Fe_3O_4$@C microsphere. Reproduced with permission from ref. 134. Copyright (2022) Royal Society of Chemistry. (b) TEM image of FeCo@C@CNGs-0.50. Reproduced with permission from ref. 135. Copyright (2019) Elsevier. (c) Schematic diagram of the process of the preparation of core–shell structured $SiO_2$@MXene@$MoS_2$ nanospheres. TEM images of (d) $SiO_2$@MXene and (e) $SiO_2$@MXene@$MoS_2$-2. Reproduced with permission from ref. 136. Copyright (2024) Wenzhou University and John Wiley & Sons. SEM images of (f) FP, and (g) and (h) FPG-4 (the FPG composites prepared using 4 mg $mL^{-1}$ GO). (i) TEM and (j) HAADF images of FPG-4. Reproduced with permission from ref. 137. Copyright (2023) Elsevier. SEM images of (k) FC-500 and (l) FC-500-M. Reproduced with permission from ref. 138. Copyright (2023) Elsevier. (m) TEM image of Co@NC@$MoS_2$-1. Reproduced with permission from ref. 139. Copyright (2022) Elsevier. (n) SEM image of CMT@CNT/Co. Reproduced with permission from ref. 140. Copyright (2019) John Wiley and Sons. (o) Schematic diagram of the preparation of FNSP and the construction of dielectric-magnetic synergies. TEM images of (p) and (q) FN (FeNi−C), (r) FNS (FeNi@$SiO_2$) and (s) FNSP. Reproduced with permission from ref. 141. Copyright (2025) Elsevier.

microspheres. This synthesis strategy effectively mitigated rGO aggregation, resulting in a homogeneous dispersion of FP particles across the rGO surface, as depicted in Fig. 9(f)–(j). For the as-prepared $Fe_3O_4$@PPy/rGO (FPG) composites, a $RL_{min}$ value of −61.20 dB was achieved at 1.89 mm. Additionally, the material demonstrated an EAB of 5.26 GHz at a matching thickness of 1.71 mm.[137] Liu *et al.* developed a dual-pathway optimization method to improve the magnetic and dielectric loss effects in the core–shell $Fe_3O_4$@C composites. By adjusting the chemical composition from $Fe_3O_4$ to metallic Fe, the

magnetic loss capacity of the FC-*x* (*x* referred to the reduction temperature) was enhanced. Additionally, by anchoring $MoS_2$ nanosheets on the surface of the carbon shell, interface polarization and dipole polarization could be provided for the Fe/$Fe_3O_4$@C@$MoS_2$ (FC-*x*-M) composites, thereby increasing the dielectric loss effect (Fig. 9(k) and (l)). The $RL_{min}$ of the FC-500-M was −36.1 dB, and the EAB was 5.4 GHz.[138] Zhang *et al.* used Co-nitrilotriacetic acid chelate nanowires (Co-NTAC) as the template and coated a layer of PDA on the surface of the Co-NTAC *via* self-polymerization. Then, the template was

removed by the hydrothermal method and Co@PDA@MoS$_2$ was obtained simultaneously. Subsequently, Co@PDA@MoS$_2$ was subjected to annealing treatment, converting PDA into NC, and a multilayer core–shell structure Co@NC@MoS$_2$ was successfully prepared (Fig. 9(m)). Thanks to the multilayer core–shell design, the impedance matching and the synergistic effect of dielectric loss and magnetic loss were optimized. Co@N-C@MoS$_2$-1 (sample with 80 mg of Na$_2$MoO$_4$·2H$_2$O and 160 mg of thiourea) exhibited an excellent EMW absorption capacity, with a RL$_{min}$ of −61.97 dB and an EAB of 5.6 GHz.[139] Wu *et al.* were the first to use sustainable biomass cotton as the template (Fig. 9(n)). By constructing layered core–shell tubular carbon/Co nanoparticle composites (CMT@CNT/Co), they achieved a

significant improvement in EMW absorption performance, with a RL$_{min}$ of −52.3 dB and an EAB of 5.1 GHz.[140] Guo *et al.* designed a hollow multilayer core–shell construction for magnetic FeNi@SiO$_2$@PPy (FNSP) nanorods (Fig. 9(o)). SEM and TEM investigations revealed that FNSP was successfully synthesized (Fig. 9(p)–(s)). The results showed that the excellent EMW absorption performance of FNSP originated from the magnetic loss in the inner layer, the enhanced conductive loss in the outermost layer of PPy, and the improved interface polarization in the middle layer of SiO$_2$. The RL$_{min}$ of FNSP was −76.38 dB, and the EAB was 5.42 GHz.[141] Jiang *et al.* utilized skin collagen fibers as templates to construct a novel multicore-shell Fe$_2$N–carbon framework anode configuration –



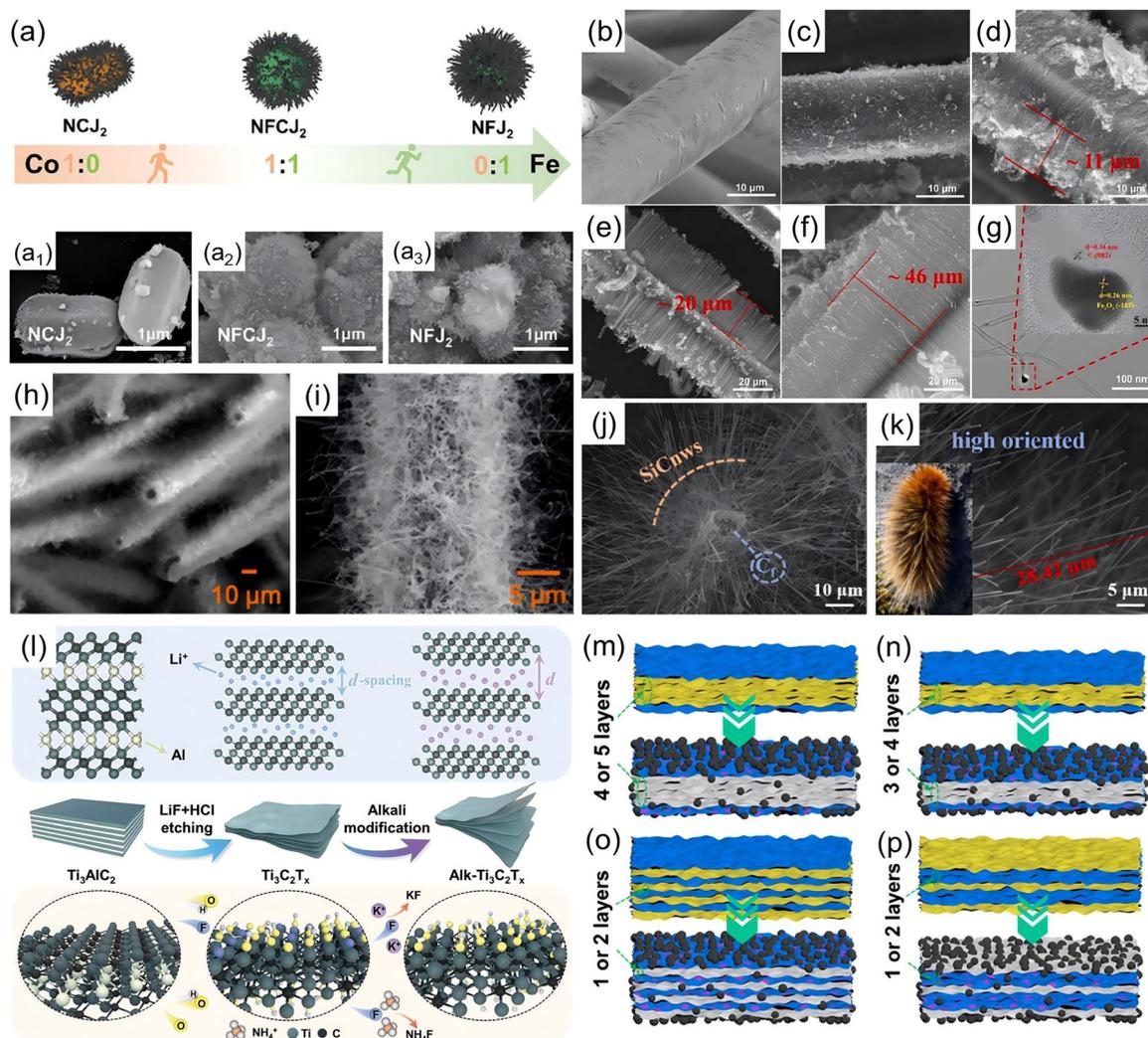**Fig. 10** (a) Material morphology changes induced by metal component, (a$_1$) NCJ$_2$, (a$_2$) NFCJ$_2$ and (a$_3$) NFJ$_2$. Reproduced with permission from ref. 144. Copyright (2024) John Wiley and Sons. (b) SEM image of desized SiC$_f$. SEM images of the CNT morphology on SiC$_f$ after various CVD reaction durations: (c) 2 min, (d) 5 min, (e) 10 min and (f) 15 min, respectively. (g) TEM images of CNTs on SiC$_f$ for 10 min. Reproduced with permission from ref. 145. Copyright (2022) Elsevier Ltd and Techna Group S.r.l. (h) and (i) FESEM graphs of SiC$_{nws}$ grown on the surface of CF. Reproduced with permission from ref. 146. Copyright (2017) American Chemical Society. (j) and (k) SEM images of the SiC$_{nws}$ array. Reproduced with permission from ref. 147. Copyright (2025) Elsevier. (l) Schematic depicting the variations in layer spacing and surface functional groups during MXene synthesis and alkali treatment. Reproduced with permission from ref. 149. Copyright (2023) John Wiley and Sons. Schematic illustration of structural units demonstrating variation with the GO/MXene ratio for different microspheres: (m) GMX1 and GMX-MFe1, (n) GMX2 and GMX-MFe2, (o) GMX3 and GMX-MFe3 and (p) GMX4 and GMX-MFe4. Reproduced with permission from ref. 150. Copyright (2023) Springer Nature.

this configuration was composed of layered nitrogen-doped carbon nanofiber bundles embedded with $Fe_2N$ nanoparticles ($Fe_2N@N$-CFBs), and achieved good electronic connection through the long-range carbon nanofiber framework, providing a favorable conductive path for electron/ion transmission.[142] The above research results have provided a new idea for constructing lightweight and highly efficient EMAs at the nanoscale.

**3.2.2. Low-dimensional nanomaterials design.** Low-dimensional nanomaterials possess an enormous specific surface area, controllable electronic structure, strong dielectric loss and designable microstructure, providing unprecedented flexibility and precise control ability for the design of EMAs.[143–151] For example, carbon nanotube regulation, orientation design of nanowire arrays, and adjustment of interlayer spacing between graphene/MXene, etc.

Yan et al. proposed a growth regulation strategy for CNTs. By altering the differential catalytic effects of Co salts and Fe salts, the growth kinetics of CNTs could be effectively controlled, and the impedance matching of the composites could be improved to produce optimal EMW absorption (Fig. 10(a)–(a$_3$)). The $RL_{min}$ of NFCJ$_2$ (the obtained black powder, F indicates $FeCl_2 \cdot 4H_2O$, C indicates $Co(NO_3)_2 \cdot 6H_2O$, and 2 represents the proportion of g-$C_3N_4$ added) at 1.76 mm was $-55.85$ dB, and the corresponding EAB was 6.35 GHz.[144] Huang et al. successfully synthesized CNT array hybrid materials with controllable lengths on silicon carbide fibers ($SiC_f$) using a floating catalyst chemical vapor deposition (CVD) method. As the duration of the CVD reaction was extended from 2 to 15 min, the lengths and densities of the CNTs changed significantly. When the CVD reaction duration was 5 min, the CNTs presented a vertical array formation on the $SiC_f$ surface, with an average length of 15 μm (Fig. 10(b)–(g)). The $RL_{min}$ of $SiC_f$-CNTs at 3 mm was $-56.2$ dB, and the EAB was 4.3 GHz.[145] The above research studies provided a new reference solution for the controllable regulation of CNTs.

The orientation design of the nanowire array is an advanced structural design strategy. By precisely controlling the arrangement direction of one-dimensional nanomaterials in three-dimensional space, it actively regulates the propagation path of EMW and their energy conversion process, thereby achieving high-performance, wide-bandwidth, thin thickness, and low-density electromagnetic absorption. Yan et al. successfully constructed a core-sheath heterostructured silicon carbide nanowires ($SiC_{nws}$) array on the surface of carbon fibers (CF) through the one-step chemical vapor infiltration method (Fig. 10(h) and (i)). Compared to CF, the $RL_{min}$ of $SiC_{nws}$-CF increased from $-5.58$ dB to $-45.98$ dB. Additionally, a conductive PPy layer was in situ coated on the surface of $SiC_{nws}$-CF ($SiC_{nws}$-CF/PPy), further increasing the $RL_{min}$ to $-50.19$ dB, and the EAB could reach 6.2 GHz. This study provided novel insight into the orientation design and fabrication of the nanowires array.[146] Deng et al. drew inspiration from biology, and using the CVD method prepared a high-oriented $SiC_{nws}$ array. By observing the cross-sectional images, it could be more clearly seen that the $SiC_{nws}$ grow radially outward along the carbon fiber cloth axis. The highly oriented needle-like nanowires are strikingly similar to the needle-like structures of the arctic woolly bear caterpillar (Fig. 10(j) and (k)). The research indicated that the $SiC_{nws}$ array constructed with $Co(NO_3)_2$ as the catalyst exhibited good EMW absorption performance. Its $RL_{min}$ was $-37.92$ dB, and the corresponding EAB was 4.59 GHz. The orientation design of these two nanowire arrays has opened up new avenues for lightweight and efficient EMA design.[147]

The control of interlayer spacing in graphene/MXene is a revolutionary structural design strategy. By precisely adjusting the internal spatial structure of the materials at the nanoscale, it fundamentally optimizes its electromagnetic parameters, thereby solving the two core problems faced by two-dimensional materials as absorbers: the high conductivity causing impedance mismatch and the single loss mechanism leading to insufficient absorption efficiency.[150] Su et al. successfully loaded thin boron nitride (BN) onto the surface of graphene through a simple process. The addition of BN might significantly increase the lamellar spacing, thus improving the interface polarization. The graphene/BN/iron/BN (graphene/BN/Fe/BN) composites benefited from the wave-transmitting property of BN, reducing the attenuation constant of the composites and optimizing the impedance matching. The absorption ability of the EMAs was effectively enhanced, with an $RL_{min}$ of $-44.53$ dB and an EAB of 4.4 GHz.[148] Du et al. successfully regulated the interlayer spacing of $Ti_3C_2T_x$ MXenes through different alkali treatments (Fig. 10(l)). Different alkali treatments have various influences on the electrical and electromagnetic properties of $Ti_3C_2T_x$. The interlayer spacing of $Ti_3C_2T_x$ treated with KOH expanded to 13.7 Å, showing a significant intercalation effect; while ammonia can provide more precise regulation. $Ti_3C_2T_x$ treated with ammonia can effectively balance the interlayer resistance, achieving efficient EMW absorption, with an $RL_{min}$ of $-49.1$ dB and an EAB of 3.9 GHz.[149] Wang et al. successfully synthesized rGO/MXene/$TiO_2/Fe_2C$ composites with a periodic intercalation structure through spray-freeze-drying and microwave radiation techniques. By varying the portion of GO to MXenes, the intercalation degree of two-dimensional nanosheets in the heterostructures could be precisely controlled to obtain excellent EMW absorption capacity. The samples were named GMX according to the mass ratio of GO to MXenes in the composites. The $RL_{min}$ of GMX-MFe3 obtained by microwave treatment of GMX3 was $-67.4$ dB at 3.1 mm, and the EAB was 5.47 GHz at 2 mm.[150] The above research provided new ideas for the controllable assembly of low-dimensional nanomaterials and their application in the field of EMW absorption (Table 2).

## 3.3. Microscale design

Microscale design can meticulously construct the geometric shape, spatial arrangement and interface relationship of materials, and regulate the propagation and conversion process of EMW at the physical level. Microscale design is the key to breaking through the performance bottlenecks of traditional absorbers. It shifts material design from being dominated by

**Table 2** EMW absorption performance of nanoscale structure absorbers

| Absorbers | $RL_{min}$ (dB) | EAB (GHz) | Thickness (mm) | Ref. |
|---|---|---|---|---|
| SiOCN | −52.93 | 3.88 | — | 115 |
| Co–CoFe$_2$O$_4$@PCHMs | −65.31 | 8.48 | — | 116 |
| SiC-T2 | −25.7 | 5 | 2 | 117 |
| Ni/C-20 | −57.25 | 5.1 | 1.8 | 118 |
| HCNS700 | −63.63 | 6.69 | — | 119 |
| HCM-2 | −34.2 | 6.1 | 2 | 120 |
| 1.2Ni-HMCNTs-800 | −56.9 | 5.95 | 2.4 | 121 |
| Ni/Ni$_2$P/CNs-2 | −72.2 | 5.8 | 1.7 | 122 |
| Porous FeNi | −60.2 | 3.38 | 1.8 | 123 |
| Co/NPC-800 | −73.87 | 6.64 | — | 125 |
| Fe/Fe$_3$Co$_7$/Co/C | −64.7 | 5.8 | 2.5 | 126 |
| ZnOCo@C | −46.77 | 6.12 | 4.6 | 127 |
| GMF | −60.13 | 6.23 | — | 128 |
| MOPCN-1/2-A | −72.9 | — | 4.4 | 130 |
| CP | −20.6 | 14.1 | 4 | 131 |
| CSC-70 | −52.82 | 8.82 | — | 132 |
| MS/MC/PNC-2 | −55.3 | 7.6 | — | 133 |
| Fe$_3$O$_4$@C | −55.4 | 9.5 | 2 | 134 |
| FeCo@C@CNGs-0.75 | −67.8 | 5.3 | — | 135 |
| SiO$_2$@MXene@MoS$_2$ | −52.11 | 5.44 | 2.4 | 136 |
| FPG | — | 5.26 | 1.71 | 137 |
| FC-500-M | — | 5.4 | 1.8 | 138 |
| Co@NC@MoS$_2$ | −61.97 | 5.6 | — | 139 |
| CMT@CNT/Co | −52.3 | 5.1 | 2 | 140 |
| FeNi@SiO$_2$@PPy | −76.38 | 5.42 | — | 141 |
| NFCJ$_2$ | −55.85 | 6.35 | 1.76 | 144 |
| SiC$_f$-CNTs | −56.2 | 4.3 | 3 | 145 |
| SiC$_{nws}$-CF/PPy | −50.19 | 6.2 | 2 | 146 |
| SiCnws array | — | 4.59 | 1.35 | 147 |
| Graphene/BN/Fe/BN | −44.53 | — | 1.5 | 148 |
| NH$_3$·H$_2$O–Ti$_3$C$_2$T$_x$ | −49.1 | 3.9 | 1.7 | 149 |
| GMX-MFe3 | −67.4 | — | 3.1 | 150 |

composition to being dominated by structure, and is the core research direction of the new generation of high-performance absorbers.

**3.3.1. Three-dimensional network structure**. The three-dimensional network structure enables EMWs to undergo multiple reflections and scattering in the materials, and increases the current transmission path, thereby enhancing the conductive loss. Additionally, the network structure can reduce the density of the materials, making it lightweight.[152–156] Three-dimensional network structure materials include aerogels, porous foams and fiber network materials, *etc.*

An aerogel can introduce a large number of pores into materials, making it more similar to the impedance of air, thereby reducing the reflection on the material's surface and allowing a greater amount of EMWs to enter the material's interior. Yang *et al.* successfully fabricated MoS$_2$/MXene aerogels using a specific porous template and atomic layer deposition technology (Fig. 11(a)). The aerogels maintained their porous structure, increased the paths for EMW reflection and scattering, and optimized the dielectric loss (Fig. 11(b)). The MoS$_2$/MXene hybrid aerogels prepared by this method exhibited a strong $RL_{min}$ of −61.65 dB.[152] Cao *et al.* have developed an ultra-light Ni-MOF-rGO aerogel that possesses advantages such as a wide frequency band, strong absorption, and lightweight thin-layer matching thickness (Fig. 11(c) and (d)). By adjusting the mass ratio of the MOF to GO, the final product exhibited a $RL_{min}$ of −51.19 dB and an EAB of 6.32 GHz.[153] Wu

*et al.* incorporated MXene nanosheets into polyacrylonitrile (PAN) nanofibers and then carried out carbonization to obtain MXene/C aerogels (MC) with a three-dimensional network structure (Fig. 11(e)). The three-dimensional network structure of the aerogels enhanced the electronic transmission efficiency, increased the conductive loss, and improved the impedance matching. The MC-2 (PAN : Ti$_3$C$_2$T$_x$ of 2 : 1) aerogel exhibited a $RL_{min}$ of −53.02 dB and an EAB of 5.3 GHz.[154]

The porous foam possesses low density, high porosity, excellent electrical conductivity and a large number of interfaces, making it an ideal EMA with integrated structural and functional properties.[156] Zhou *et al.* successfully prepared a novel kind of MoS$_2$/CNT carbon foam (MC@CF). By altering the portion of MoS$_2$/CNT in MC@CF, the EMW absorption performance could be significantly regulated. When the mass fraction of MoS$_2$/CNT is 3%, the $RL_{min}$ of MC@CF was −68.7 dB. Its excellent EMW absorption capability was attributed to the three-dimensional interconnected porous architecture and multiple heterogeneous interface effects.[155] Zhang *et al.* successfully synthesized carbon nanowires (CNC) on three-dimensional carbon foam (CF), and then mixed them with FeNi/NiFe$_2$O$_4$ to form a new type of FeNi/NiFe$_2$O$_4$/CNC/CF (FCCF) ternary composite foams (Fig. 11(f)–(i)). The $RL_{min}$ of the FCCF-2 (a precursor solution with a concentration of 1.5 times that of the original solution) composite foam reached −53 dB, and the broad EAB was 10 GHz. Its remarkable EMW absorption performance was attributed to the synergistic effect of its dielectric property, chirality, and magnetism.[156]

The fiber network structure is more likely to form an effective three-dimensional conductive network at a lower filling content, thereby achieving efficient and controllable conductive loss. Meanwhile, many fibers inherently exhibit excellent conductive loss and magnetic loss capabilities, making them potential materials for constructing advanced EMAs. Xiang *et al.* successfully fabricated SiC nanofibers (SC) through electrospinning and carbonization treatment. Subsequently, magnetic component Fe$_3$Si was introduced into the SC. By varying the addition amount of polycarbosilane (PCS), the EMW absorption ability of the SiC@Fe$_3$Si (SC-F) was significantly enhanced. When the content of PCS was 5.3 wt%, the SC3-F demonstrated remarkable EMW absorption ability, with a $RL_{min}$ of −73.75 dB. The formation of a three-dimensional conducting system and an increase in magnetic loss had a significant impact on enhancing of the EMW absorption ability (Fig. 11(j)).[157] Wu *et al.* successfully constructed MOF-derived Cu$_9$S$_5$/C nanocomposite fibers through a three-step process of electrospinning, carbonization, and sulfidation. The study of the SEM images revealed that Cu$_9$S$_5$/C was uniformly distributed within the carbon fibers, forming a unique three-dimensional network structure (Fig. 11(k) and (l)). The three-dimensional conductive network played a crucial part in improving the electrical conductivity of the MOF derivative and optimizing the conductive loss of the composites. When the loading amount of Cu-MOF was 40 wt%, the $RL_{min}$ of Cu$_9$S$_5$/C-40 reached −69.6 dB, and the EAB reached 5.81 GHz.[158] The above research has revealed that the design of the
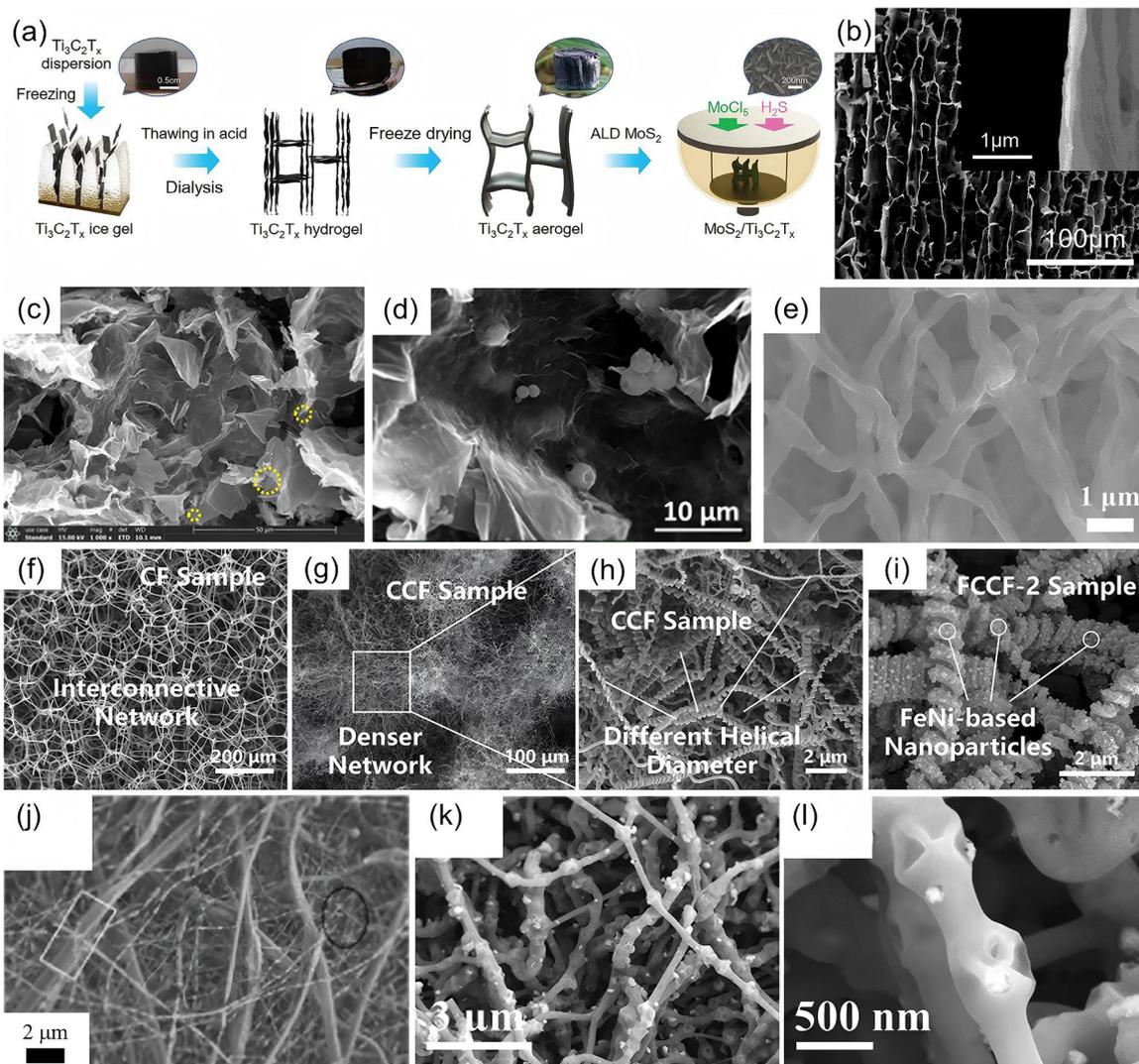
**Fig. 11** (a) Schematic illustration of the preparation process for the MoS$_2$/MXene hybrid aerogel. (b) SEM image of the transverse section of the Ti$_3$C$_2$T$_x$ aerogel. Reproduced with permission from ref. 152. Copyright (2022) John Wiley and Sons. (c) and (d) SEM images of the 600Ni-rGO aerogel. Reproduced with permission from ref. 153. Copyright (2023) American Chemical Society. (e) SEM image of the MC-2 aerogel. Reproduced with permission from ref. 154. Copyright (2023) Springer Nature. SEM images of the (f) CF sample, (g) and (h) CCF sample, and (i) FCCF-2 sample. Reproduced with permission from ref. 156. Copyright (2025) Springer Nature. (j) SEM image of SC3-F. Reproduced with permission from ref. 157. Copyright (2025) Elsevier. (k) and (l) SEM images of Cu$_9$S$_5$/C-40. Reproduced with permission from ref. 158. Copyright (2024) Donghua University.

three-dimensional conductive network provides a theoretical basis for the construction of optimal EMAs.

**3.3.2. Other structures.** In microscale design, apart from the common construction of a three-dimensional network structure, there are also other structures that can make significant contributions to the efficient absorption of EMW, such as a layered structure,[159] biomimetic structure,[162] and oriented arrangement structure,[165] *etc.*

Layered structure materials possess large specific surface areas and interlayer interfaces. EMW will undergo multiple reflections and scattering at the gaps or interfaces between layers, thereby increasing the chances of EMW being absorbed. Gu *et al.* successfully prepared MXene/CNTs/polyimide (MCP) aerogels with a multilayered structure *via* a bidirectional

freeze-casting method. Morphological results indicated that the MCP3 (MXene : CNT : polyamic acid = 3 : 1 : 6) aerogel was composed of a layered structure with parallel-aligned multi-layered components (Fig. 12(a)–(c)). This unique structure could significantly reduce the heat transfer between layers, promote heat dissipation, and achieve an ultralow thermal conductivity of 15.3 mW m$^{-1}$ K$^{-1}$. Meanwhile, the RL$_{min}$ of this aerogel was −75.8 dB, and the EAB was 7.14 GHz.[159] Deng *et al.* constructed SiOC/ZrB$_2$ reinforced ZrO$_2$/SiO$_2$ layered composites. The (ZrO$_2$–SiO$_2$)$_f$/ZrB$_2$–SiOC composites had a continuous multi-layer structure and exhibited excellent oxidation resistance and thermal insulation properties, indicating their potential application value in complex environments (Fig. 12(d)). The RL$_{min}$ of the composites was −59.34 dB, and
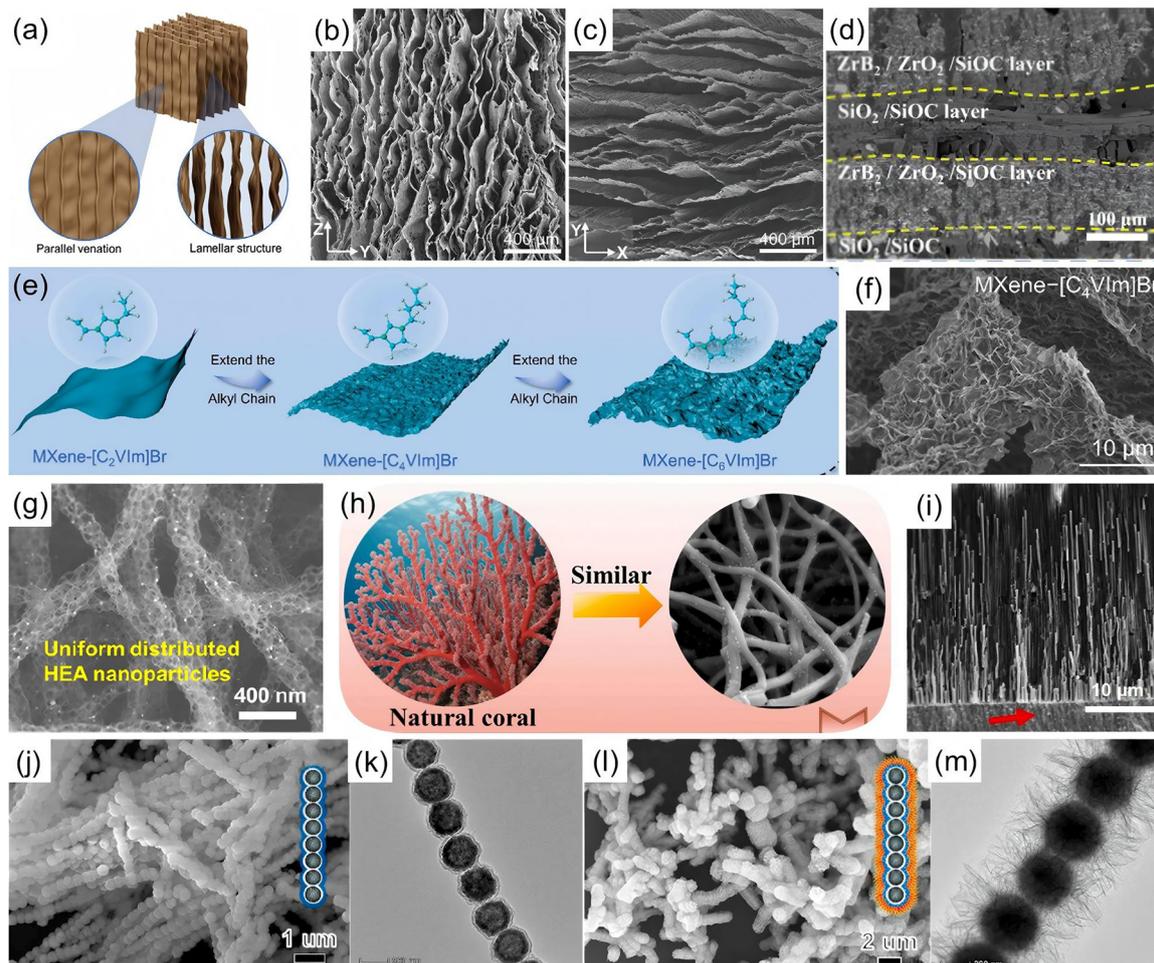
**Fig. 12** (a) Schematic diagram of the MXene/CNTs/PI aerogel. (b) and (c) Anisotropic structure of MCP3. Reproduced with permission from ref. 159. Copyright (2024) John Wiley and Sons. (d) Cross-section SEM images of the $(ZrO_2-SiO_2)_f/ZrB_2-SiOC$ composites. Reproduced with permission from ref. 160. Copyright (2024) Elsevier. (e) Schematic diagram of MXene-IL aerogels with different alkyl chain lengths. (f) SEM image of the MXene$-[C_4VIm]Br$ hybrid aerogel. Reproduced with permission from ref. 161. Copyright (2025) Elsevier. (g) SEM image of the synthesized HCNF/HEA composite. Reproduced with permission from ref. 162. Copyright (2024) American Chemical Society. (h) Schematic diagram and SEM image of FeC/C nanofibers with a bionic coral-like network structure. Reproduced with permission from ref. 163. Copyright (2025) Elsevier. (i) SEM image of FeCo@AAO-2. Reproduced with permission from ref. 164. Copyright (2025) Elsevier Ltd and Techna Group S.r.l. (j) SEM and (k) TEM images of the $Fe_3O_4@void@mSiO_2$ composites. (l) SEM and (m) TEM images of the $Fe_3O_4@void@mSiO_2@MnO_2$ composites. Reproduced with permission from ref. 165. Copyright (2021) Elsevier.

the EAB was 4.2 GHz.[160] Zhang *et al.* utilized the solution self-assembly strategy and employed ionic liquids (IL) as cross-linking agents to successfully prepare an MXene-IL aerogel featuring an internal layered structure in the form of a wrinkled shape (Fig. 12(e) and (f)). The results showed that the microscopic layered folds in the aerogel may be precisely regulated by adjusting the alkyl side chain length of the ionic liquid. The EAB of the aerogel reached 6.12 GHz. This study achieved the controllable regulation of the microscopic structure of MXenes.[161]

Biological structures in nature have evolved many efficient energy management structures (including light, sound, heat and force) for survival and adaptation to the environment. Biomimetic structure design precisely provides solutions to problems such as high density, thick thickness and poor

mechanical properties. Introducing honeycomb, coral, *etc.* structures into EMAs can form a good conductive network and significantly reduce the material's density, meeting the strict lightweight requirements in various fields.[162,163] Wang *et al.* used honeycomb-like porous nanofibers (HCNF) as the base materials and successfully combined the FeCoNiCuMn high-entropy alloys (HEA) with HCNF through an electrospinning and Joule heating method to fabricate the HEA/C materials derived from HCNF/HHA (Fig. 12(g)). Thanks to its honeycomb structure and lattice distortion effect, the composites exhibited excellent EMW absorption capacity, with a $RL_{min}$ of −65.8 dB and an EAB of 7.68 GHz.[162] Hu *et al.* drew inspiration from the structure of corals and successfully fabricated FeC/C nanofibers with a coral-like multi-branch network structure through electrospinning combined with a

carbonization process (Fig. 12(h)). The $RL_{min}$ of the composite nanofibers was −67.24 dB, and the EAB was 5.24 GHz. The excellent EMW absorption performance was attributed to the bionic coral structure, which optimized the multiple scattering paths and impedance matching of EMWs.[163]

The oriented structure arrangement can precisely control the electromagnetic loss path through the orderly design of the microstructure, thereby breaking through the performance bottleneck of disordered composites. Zhu et al. successfully fabricated a three-electrode electrochemical deposition method assisted by a template to produce the three-dimensional nanowire arrays of FeCo@anodic aluminum oxide (AAO). Morphological analysis revealed that the nanowires grew directionally within the pores of the AAO template (Fig. 12(i)). By altering the Fe/Co atomic ratio in the composites, the electromagnetic parameters could be precisely controlled, achieving advanced EMW absorption capabilities with a $RL_{min}$ of −61.9 dB.[164] Qiao et al. effectively created a chain-like structure of $Fe_3O_4$@void@$mSiO_2$@$MnO_2$ composites. The cross-linked chain structure provided favorable conditions for the multiple scatterings and reflection of EMW (Fig. 12(j)–(m)). Compared with the $Fe_3O_4$@void@$mSiO_2$ composites, the introduction of the $MnO_2$ shell layer helped to increase the porosity. Besides, the BET specific surface area increased from 125.45 $m^2\ g^{-1}$ to 201.50 $m^2\ g^{-1}$, and the $RL_{min}$ was −45.76 dB[165] (Table 3).

### 3.4. Macroscale design

Macroscale design is the core approach for EMAs to achieve practical engineering applications. It no longer focuses solely on the chemical composition of the materials themselves, but instead manages and controls EMWs by constructing macroscopic physical structures, thereby achieving breakthroughs in EMW absorption performance. Moreover, macroscale design elevates EMAs from simple functional coatings to functional devices, addressing stringent engineering demands for lightweight construction, high strength, and environmental stability. Typical macroscale designs include periodic structures, frequency selective surfaces and impedance gradient structures, etc.

**3.4.1. Periodic structures and frequency selective surfaces.** Periodic structures endow materials with new functions beyond their intrinsic properties. By controlling the geometric shape, size and arrangement period of their constituent units, structural resonance and interference cancellation can be achieved.[167,168] Liu et al. used flexible platinum-catalyzed silicone rubber as the substrates and meticulously developed an elastic EMA with dome array structures (Fig. 13(a)). Through the gradual increase of the deformation caused by pressure stimulation, the macro-dome architecture gradually flattened out, which was conducive to the reduction of the interlayer spacing of the tiny conductive network layer and the development of fresh conductive paths. The EAB of the composites was 5.16 GHz.[166] Choi et al. designed a periodic pattern coated glass fabric (PPCF) using a carbon-based conducting material bar coating device (Fig. 13(b) and (c)). This material exhibited optimal EMW absorption performance within the EAB of

**Table 3** EMW absorption performance of microscale structure absorbers

| Absorbers | $RL_{min}$ (dB) | EAB (GHz) | Filler ratio (wt%) | Ref. |
|---|---|---|---|---|
| $MoS_2$/MXene | −61.65 | 5.9 | — | 152 |
| 600Ni-rGO | −51.19 | 6.32 | 2 | 153 |
| MXene/C | −53.02 | 5.3 | 15 | 154 |
| $MoS_2$/CNT | −68.7 | 14.9 | — | 155 |
| FCCF-2 | −53 | 10 | — | 156 |
| SC3-F | −73.75 | 4.4 | 30 | 157 |
| $Cu_9S_5$/C-40 | −69.6 | 5.81 | 20 | 158 |
| MXene/CNTs/PI | −75.8 | 7.14 | 2.4 | 159 |
| $(ZrO_2–SiO_2)_f$/$ZrB_2$–SiOC | −59.34 | 4.2 | — | 160 |
| MXene-IL | −42.05 | 6.12 | 1.38 | 161 |
| HCNF/HEA | −65.8 | 7.68 | 2 | 162 |
| FeC/C | −67.24 | 5.24 | 30 | 163 |
| FeCo@AAO | −61.9 | 4 | 80 | 164 |
| $Fe_3O_4$@void@$mSiO_2$@$MnO_2$ | −45.76 | 5.13 | 40 | 165 |

4 GHz. In addition, PPCF also exhibited good interlayer shear strength.[167] Ma et al. prepared a periodic array structure of magnetic-dielectric synergistic gradient materials (MDSGM) consisting of an oriented flaky carbonyl iron (FCI) film and a periodic array of RGO/CNT/CNF aerogel (GTFA) (Fig. 13(d) and (e)). The MDSGM achieved multispectral ultra-wideband EMW absorption performance, with a $RL_{min}$ of −40.24 dB and an average RL value of −19.3 dB.[168]

The construction of FSS is like an electromagnetic sieve, whose characteristics determine that it can only reflect or transmit waves within specific frequency bands. Combined with the underlying absorber structure, it is possible to design intelligent and highly efficient EMAs for specific frequency bands. Yang et al. designed and fabricated a double-layer ultra-thin broadband radar absorber structure (RAS), with the FSS on the top layer and a dielectric ceramic coating on the bottom layer (Fig. 13(f)). This study systematically revealed the influence of key design parameters such as the size and period of the FSS on the EMW absorption performance of the RAS. The results showed that by optimizing the size of the FSS, the EMW absorption capability of the RAS can be significantly enhanced, ultimately extending the EAB to 7 GHz.[169] Zhang et al. successfully designed multi-layer FSS broadband EMAs. This absorber featured two layers of FSS (Fig. 13(g) and (h)). By collaboratively optimizing the materials parameters and geometric configurations of the surface, the absorber exhibited an absorption rate exceeding 90% within the frequency range of 3.1–18 GHz.[170] Yang et al. successfully prepared $Cr_2O_3$–$TiO_2$ (CrTiO) composite coatings with different $Cr_2O_3$ contents using high-temperature solid-phase reaction and plasma spraying technology (Fig. 13(i)–(k)). The study confirmed that by controlling the content of $Cr_2O_3$ and the overall thickness of the coating, efficient EMW attenuation could be achieved. Furthermore, it was found that constructing the FSS composed of circular and square elements on the surface of the CrTiO coating could significantly optimize its EMW absorption performance.[171]

**3.4.2. Impedance gradient design and other structures.** Impedance gradient design is a strategy that involves making the electromagnetic parameters of the material vary continuously or in steps from the surface to the interior, in order to
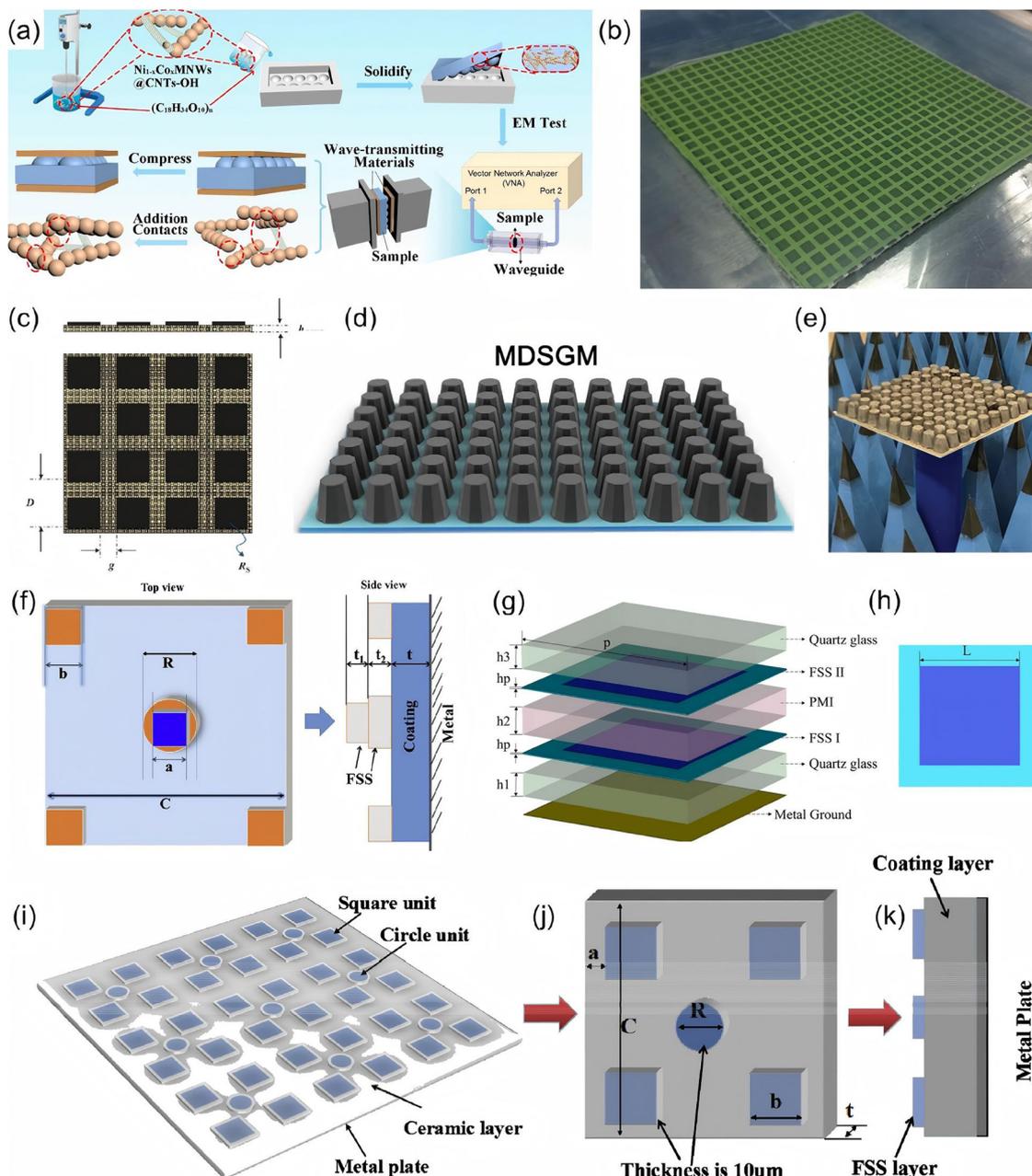
**Fig. 13** (a) A schematic representation of the fabrication and deformation processes of the elastic EMAs featuring macro-dome array structures. Reproduced with permission from ref. 166. Copyright (2025) Elsevier. (b) PCCF absorber. (c) Geometry of the EMW absorption structure using PPCF with design variables. Reproduced with permission from ref. 167. Copyright (2020) Elsevier. (d) Model diagram of MDSGM consisting of a GTFA unit and oriented FCI film. (e) Images of MDSGM. Reproduced with permission from ref. 168. Copyright (2024) John Wiley and Sons. (f) Schematic structure of the FSS unit cell. $C$ is the period of the FSS, $R$ is the diameter of the circle, $a$ and $b$ are the side lengths of the square including in the first and the second layer FSS, respectively. $t_1$, $t_2$ and $t$ are the thicknesses of the first and second layer FSS, and the coating, respectively. Reproduced with permission from ref. 169. Copyright (2017) Elsevier. (g) Unit-cell structure of the proposed MMA. (h) Schematic illustration of the FSS. Reproduced with permission from ref. 170. Copyright (2025) Elsevier. (i)−(k) Designed absorbing materials model. Reproduced with permission from ref. 171. Copyright (2019) Elsevier.

achieve a smooth transition of wave impedance to free space. This strategy aims to minimize the surface reflection of EMW, thereby creating the prerequisite for efficient loss within the material. Li *et al.* constructed MXene/rGO films with a vertical heterogeneous structure, successfully achieving impedance gradient control. The simulation results in Fig. 14(a) illustrate

a diagram of the electrical field distribution of each single layer of the different films. The color of the electric field distribution is redder, indicating stronger conductivity. By adjusting the content of GO, effective control of EMW absorption was achieved, with an $RL_{min}$ of −44.3 dB and an EAB of 4.84 GHz.[172] Duan *et al.* studied and prepared three types of
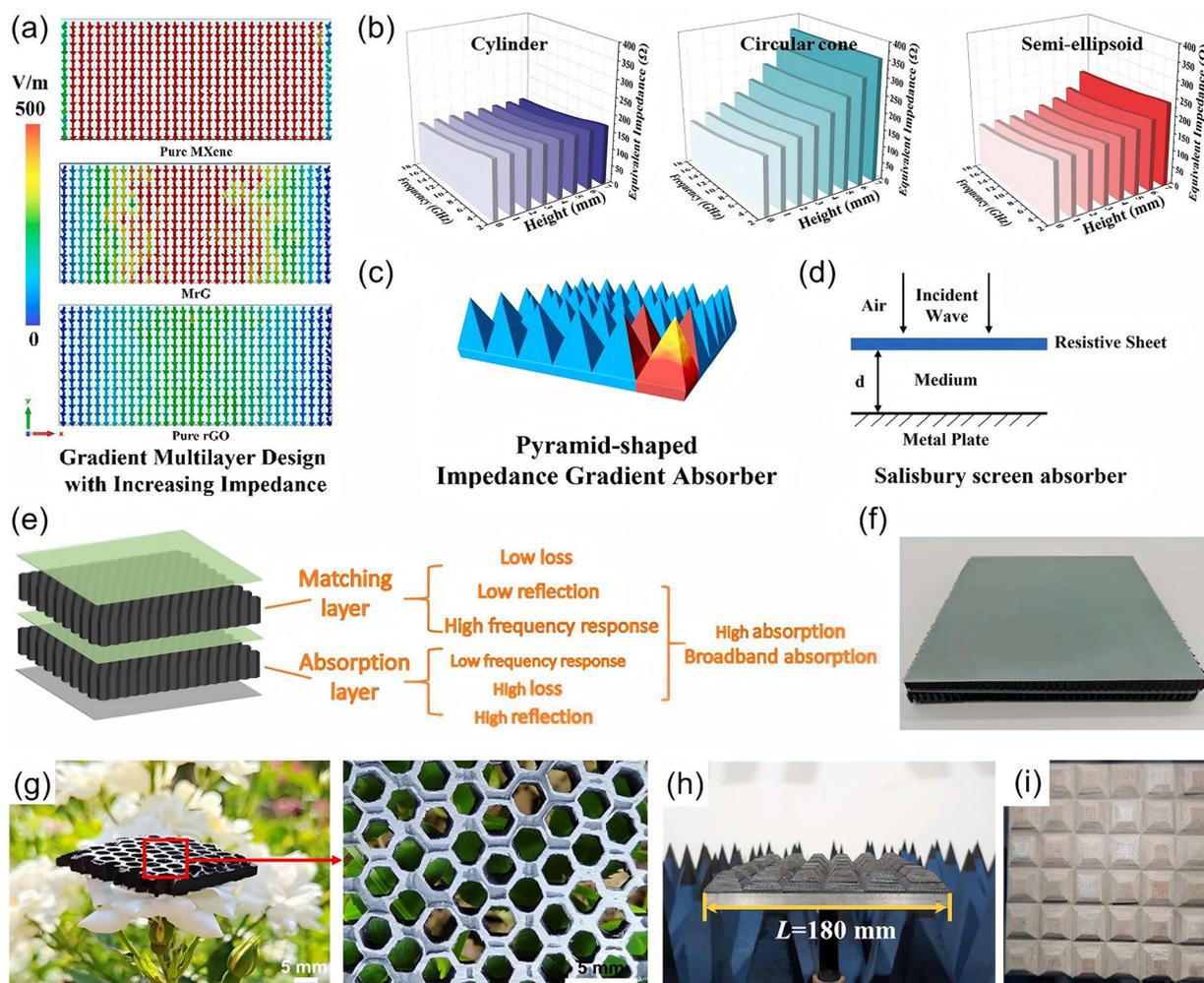
**Fig. 14** (a) Simulated electrical fields of pure MXene, MrG (with 80 wt% rGO content) and pure rGO films. Reproduced with permission from ref. 172. Copyright (2023) Elsevier. (b) The equivalent impedance at various heights of the substrate of the moth eye biomimetic materials with the top structure height of 8 mm. Reproduced with permission from ref. 173. Copyright (2023) John Wiley and Sons. Schematic diagram of the (c) pyramid–shaped impedance gradient absorber and (d) Salisbury screen absorber. Reproduced with permission from ref. 174. Copyright (2023) Elsevier. (e) Schematic of the gradient honeycomb sandwich structure. (f) Gradient honeycomb sandwich architecture. Reproduced with permission from ref. 175. Copyright (2025) Elsevier. (g) Digital image of MAAH. Reproduced with permission from ref. 176. Copyright (2024) Donghua University. (h) The EMW absorption property test image of the material at room temperature. (i) The digital image of the material. Reproduced with permission from ref. 177. Copyright (2026) Elsevier.

carbonic iron (CIP)/polyurethane (PU) EMAs with cylinder, circular cone and semi-ellipsoid structures (Fig. 14(b)). The results showed that by constructing a gradient impedance inside the absorbers, the EMW absorption capacity could be substantially increased. The EAB of the semi-ellipsoid architecture absorber could reach 6.94 GHz.[173] Deng *et al.* successfully fabricated polyamide@C/Fe$_3$O$_4$ fibers (PCF) by combining melt spinning and three-dimensional weaving techniques (Fig. 14(c) and (d)). PCF could be easily woven into diverse three-dimensional textiles, achieving impedance gradient and interference cancellation simultaneously. The EMW absorption performance could be regulated by changing the structural size of PCF. Ultimately, the PCF exhibited an RL$_{min}$ of −47.51 dB and an EAB of 5.2 GHz.[174]

Wu *et al.* prepared a dual-response synergistic gradient honeycomb sandwich structure (GHSS) which exhibited

excellent broadband absorbing performance. The gradient structure optimized the impedance matching between the honeycomb structure and the air, and the dual-response synergistic mechanism further widened the bandwidth (Fig. 14(e) and (f)). Together, these two mechanisms ensure comprehensive and reliable absorption across the 2–18 GHz wide frequency range.[175] The EMW absorption aramid honeycomb (MAAH) composed of MXene nanosheets and aramid nanofibers (ANFs) was successfully developed by Sun *et al.* (Fig. 14(g)). With the RL$_{min}$ of −38.5 dB, MAAH's EMW absorption performance was improved by the formation of a three-dimensional conductive network and the combined action of the honeycomb multi-level structure. In the meantime, MAAH's compressive strength was also improved by the dense network structure.[176] A frustum pyramid structure SiCf/SiBCN composite was devised and successfully manufactured by Huang *et al.*

Table 4 EMW absorption performance of macroscale structure absorbers

| Absorbers | $RL_{min}$ (dB) | EAB (GHz) | Thickness (mm) | Ref. |
|---|---|---|---|---|
| NiCo chains/CNTs-OH | −34.93 | 5.16 | 1.55 | 166 |
| PPCF | −27 | 4.2 | — | 167 |
| MDSGM | −40.24 | — | — | 168 |
| RAS | −27.5 | ∼7 | — | 169 |
| MMA | — | 14.9 | 8.45 | 170 |
| CrTiO | — | 4.2 | 1.9 | 171 |
| MXene/rGO | −44.3 | 4.84 | — | 172 |
| CIP/PU | — | 6.94 | 3 | 173 |
| Polyamide@C/$Fe_3O_4$ | −47.51 | 5.2 | — | 174 |
| GHSS | −29 | 16 | 21 | 175 |
| MAAH | −38.5 | — | 1.9 | 176 |
| $SiC_f$/SiBCN | −33.4 | 12.5 | — | 177 |

(Fig. 14(h) and (i)). The composite showed a great synergistic effect of EMW absorption at both room temperature and high temperatures following structural optimization and geometric parameter adjustment. The EAB was 34.8 GHz (5.2–40 GHz) at ambient temperature and remained at 12.5 GHz (5.5–18 GHz) at 1100 °C[177] (Table 4).

## 4. Conclusion and outlook

Multi-scale structural design and optimization of EMAs play a crucial role in enhancing their performance. This paper systematically reviews recent research advances in improving EMA performance through multi-scale structural design, providing a theoretical basis for optimizing the properties of different structural materials. Research indicates that material structure ranging from atomic arrangement to macroscopic configuration, has become the core approach for pushing beyond the performance limits of traditional EMAs. Structural design plays a decisive role in determining their electromagnetic parameters, impedance matching characteristics and loss mechanisms. At the atomic/molecular scale, atomic dispersion and defect engineering significantly enhance dielectric loss and charge transport capabilities by precisely optimizing the intrinsic electromagnetic parameters of materials, such as electronic structure and localized polarization. At the nanoscale, the construction of hollow, porous, core–shell structures and low-dimensional nanomaterials not only achieves lightweight design, but also significantly enhances the electromagnetic energy dissipation efficiency through multiple reflections, interface polarization and the synergistic effect of magnetism and dielectricity. At the microscale, a three-dimensional network, layered structure and biomimetic designs effectively coordinate impedance matching and attenuation performance by regulating EMW propagation paths and the distribution of a conductive network. At the macroscale, the building of periodic structures, FSS and gradient structures has further enabled the active management of EMW propagation and broadband absorption, accelerating the development of EMAs towards intelligence, device integration, and system-level integration. These structural design strategies, through the synergistic effect of multiple levels and multiple mechanisms, significantly enhance the comprehensive performance of the materials,

providing a reliable path for achieving high-performance EMAs with properties such as lightweight, wide bandwidth, and robust absorption.

Although multi-scale structural design has achieved significant results in the area of EMAs, the development of advanced EMAs still faces numerous challenges and opportunities to meet the diverse demands of next-generation electromagnetic protection technologies.

(1) Current structures predominantly feature static designs. Future development must focus on creating smart materials (such as phase-change materials and liquid crystal composites) capable of responding to environmental stimuli including temperature, electric fields and stress. This will enable dynamic control over absorption bandwidth and intensity, meeting the demands of complex electromagnetic environments and adaptive stealth requirements.

(2) The current preparation techniques still have limitations in the precise control of cross-scale structures and large-scale production. In the future, advanced methods such as atomic manufacturing (e.g., scanning probe technology), 4D printing and template self-assembly should be combined to achieve controllable preparation from atomic to macro structures. At the same time, the application of multi-physics field simulation, machine learning and AI in material design should be strengthened. Through cross-scale modeling and big data analysis, the discovery and optimization of new material systems can be accelerated.

(3) The materials should develop towards a direction of structural–function integration, maintaining efficient absorption performance while integrating functions such as thermal management, load-bearing, and corrosion resistance. Especially in fields like aerospace and flexible electronics, it is necessary to focus on solving the stability and durability issues of the materials under extreme conditions (high temperature, corrosion and mechanical load).

(4) While striving for high performance, the full life-cycle impact of materials must also be taken into account. Developing environmentally friendly, biocompatible, and even biodegradable green absorbers, as well as exploring low-energy consumption and low-pollution sustainable production processes, will be inevitable requirements for the long-term healthy development of this field.

## Author contributions

Yang Guan: conceptualization, information collection, and writing original draft. Yongpeng Wu, Jianyu Zhou, Kai Yao, and Ruolin Liu: information collection and writing original draft. Yang Yang and Wei Lu: conceptualization, writing (editing), supervision, and project administration.

## Conflicts of interest

There are no conflicts to declare.

## Data availability

No primary research results, software or code have been included and no new data were generated or analysed as part of this review.

## Acknowledgements

## Notes and references

1 X. Zhang, X. Tian, N. Wu, S. Zhao, Y. Qin, F. Pan, S. Yue, X. Ma, J. Qiao, W. Xu, W. Liu, J. Liu, M. Zhao, K. Ostrikov and Z. Zeng, *Sci. Adv.*, 2024, **10**, eadl6498.
2 M. Ying, R. Zhao, X. Hu, Z. Zhang, W. Liu, J. Yu, X. Liu, X. Liu, H. Rong, C. Wu, Y. Li and X. Zhang, *Angew. Chem., Int. Ed.*, 2022, **61**, e202201323.
3 F. Pan, Y. Shi, Y. Yang, H. Guo, L. Li, H. Jiang, X. Wang, Z. Zeng and W. Lu, *Adv. Mater.*, 2024, **36**, 2311135.
4 L. Liang, W. Gu, Y. Wu, B. Zhang, G. Wang, Y. Yang and G. Ji, *Adv. Mater.*, 2022, **34**, 2106195.
5 K. Yao, L. Song, X. Zhang, L. Li, F. Pan, Y. Yang, J. Liang, J. Wang, B. Yuan and W. Lu, *Sci. Adv.*, 2025, **11**, eaea0362.
6 Z. Zhao, Y. Qing, L. Kong, H. Xu, X. Fan, J. Yun, L. Zhang and H. Wu, *Adv. Mater.*, 2024, **36**, 2304182.
7 Z. Wu, H. Cheng, C. Jin, B. Yang, C. Xu, K. Pei, H. Zhang, Z. Yang and R. Che, *Adv. Mater.*, 2022, **34**, 2107538.
8 Z. Wei, Z. Li, D. Chen, J. Liang and J. Kong, *Small Struct.*, 2025, **6**, 2400615.
9 Y. Liu, J. Zhou, C. Li, H. Zhang, Y. Wang, Y. Yan, L. Duan, Z. Cheng, Y. Ma and Z. Yao, *Nat. Commun.*, 2025, **16**, 202.
10 N. Qu, H. Sun, Y. Sun, M. He, R. Xing, J. Gu and J. Kong, *Nat. Commun.*, 2024, **15**, 5642.
11 J. Yan, Y. Huang, X. Liu, X. Zhao, T. Li, Y. Zhao and P. Liu, *Polym. Rev.*, 2021, **61**, 3.
12 L. Kong, S. Zhang, Y. Liu, H. Wu, X. Fan, Y. Cao and J. Huang, *Carbon*, 2023, **207**, 198–206.
13 Y. Liu, X. Qi, X. Deng, J. Ye, Y. Fu and S. Fu, *ACS Appl. Mater. Interfaces*, 2023, **15**, 28491–28502.
14 S. Hou, Y. Wang, F. Gao, H. Yang, F. Jin, L. Ren, Q. Wu, H. Ge and Y. Wang, *Chem. Eng. J.*, 2023, **471**, 144779.
15 M. Qin, L. Zhang, X. Zhao and H. Wu, *Adv. Funct. Mater.*, 2021, **31**, 2103436.
16 Y. Guo, K. Ruan, G. Wang and J. Gu, *Sci. Bull.*, 2023, **68**, 1195–1212.
17 C. Liang, Z. Gu, Y. Zhang, Z. Ma, H. Qiu and J. Gu, *Nano-Micro Lett.*, 2021, **13**, 181.
18 Z. Li, W. Yang, B. Jiang, C. Wang, C. Zhang, N. Wu, C. Zhang, S. Du, S. Li, H. Bai, X. Wang and Y. Li, *ACS Appl. Mater. Interfaces*, 2023, **15**, 7578–7591.
19 X. Liu, M. Ji and J. Shao, *RSC Adv.*, 2021, **11**, 26056.
20 R. Shu, Y. Guan and B. Liu, *J. Mater. Sci. Technol.*, 2025, **214**, 16–26.
21 Y. Guo, Y. Duan, X. Liu, Y. Shi, Z. Fan, H. Pang and L. Pan, *J. Mater. Sci. Technol.*, 2025, **237**, 288–297.
22 M. Zhang, S. Fang, A. A. Zakhidov, S. B. Lee, A. E. Aliev, C. D. Williams, K. R. Atkinson and R. H. Baughman, *Science*, 2005, **309**, 1215–1219.
23 B. Huang, X. Chen, Y. Wang, Y. Liu, J. Zhou, Y. Liu and J. Yue, *Ceram. Int.*, 2023, **49**, 36715–36723.
24 J. Xu, X. Zhang, H. Yuan, S. Zhang, C. Zhu, X. Zhang and Y. Chen, *Carbon*, 2020, **159**, 357–365.
25 Y. Wu, Y. Zhao, M. Zhou, S. Tan, R. Peymanfar, B. Aslibeiki and G. Ji, *Nano-Micro Lett.*, 2022, **14**, 171.
26 X. Luo, H. Xie, J. Cao, Y. Lu, S. Tao, Z. Meng, L. Pu, L. Sun, P. He and Z. Liu, *RSC Adv.*, 2024, **14**, 10687.
27 J. Shu, M. Cao, Y. Zhang, Y. Wang, Q. Zhao, X. Fang, S. Yang, Y. Qin and J. Yuan, *Adv. Funct. Mater.*, 2023, **33**, 2212379.
28 L. Cai, H. Jiang, F. Pan, H. Liang, Y. Shi, X. Wang, J. Cheng, Y. Yang, X. Zhang, Z. Shi, H. Wu and W. Lu, *Small*, 2024, **20**, 2306698.
29 K. Yao, F. Pan, H. Liang, X. Zhang, L. Li, L. Song, Y. Yang, B. Yuan and W. Lu, *Adv. Funct. Mater.*, 2025, **35**, 2413639.
30 L. Li, F. Pan, H. Guo, H. Jiang, X. Wang, K. Yao, Y. Yang, B. Yuan, I. Abdalla, R. Che and W. Lu, *Small*, 2024, **20**, 2402564.
31 H. Wang, J. Bi, J. Wang, Y. Sha, Z. Liu, C. Wang and L. Qian, *Mater. Today Phys.*, 2025, **58**, 101852.
32 J. Li, S. Chen, R. Fan, X. Gong, H. Zhao, L. Yan and Y. Zhou, *Carbon*, 2024, **224**, 119058.
33 P. Zhang, X. Zhang, B. Li, L. Xu, F. Dang and B. Li, *Adv. Compos. Hybrid Mater.*, 2021, **4**, 1292–1301.
34 Y. Shi, H. Liu, N. Tian and C. You, *J. Mater. Sci. Technol.*, 2026, **258**, 22–44.
35 W. Yu and G. Shao, *J. Colloid Interface Sci.*, 2023, **640**, 680–687.
36 J. Xiao, X. Qi, L. Wang, T. Jing, J. Yang, X. Gong, Y. Chen, Y. Qu, Q. Peng and W. Zhong, *Nano Res.*, 2023, **16**, 5756–5766.
37 Q. Li, D. Liang, D. Wang, L. Ling, L. Jiang, F. Qiu and M. Qian, *Mater. Today Commun.*, 2024, **38**, 107862.
38 H. Ding, W. Song, Y. Chen, Y. Wang, Y. Wang, C. Tian and Y. Du, *Carbon*, 2025, **244**, 120621.
39 R. Xu, D. Xu, Z. Zeng and D. Liu, *Chem. Eng. J.*, 2022, **427**, 130796.
40 J. Liu, J. Dong, M. Tang, Y. Si, Y. Wang and R. Sun, *Mater. Des.*, 2025, **257**, 114420.
41 C. Gao, D. Gou, G. Huang, Z. Zhang, J. Wei, F. Gao, Y. Zhang, M. Terrones, X. Chen and Y. Wang, *Nano Energy*, 2025, **138**, 110863.
42 Z. He, Y. Shi, H. Wang and Y. Zhu, *Compos. Sci. Technol.*, 2024, **257**, 110826.

43 Y. Zhang, Y. Xie, W. Yang, G. Wu, S. Chen and Y. Wang, *Colloids Surf., A*, 2024, **696**, 134270.

44 T. Liu, Y. Mu, X. Geng, S. Han and S. Huang, *J. Alloys Compd.*, 2025, **1035**, 181399.

45 Q. An, D. Li, W. Liao, T. Liu, D. Joralmon, X. Li and J. Zhao, *Adv. Mater.*, 2023, **35**, 2300659.

46 Z. Ma, K. Yang, D. Li, H. Liu, S. Hui, Y. Jiang, S. Li, Y. Li, W. Yang, H. Wu and Y. Hou, *Adv. Mater.*, 2024, **36**, 2314233.

47 Y. Ma, S. Wei, R. Liu, L. Sun and W. Wang, *J. Mater. Chem. C*, 2024, **12**, 9068.

48 X. Zhang, S. Guo, G. Wei, H. Zhang, X. Hao, S. Tan, K. Liu and G. Ji, *Composites, Part B*, 2025, **306**, 112798.

49 I. Hussain and S. Yesmin, *Mater. Chem. Phys.*, 2023, **309**, 128337.

50 H. Jiang, B. Yuan, H. Guo, F. Pan, F. Meng, Y. Wu, X. Wang, L. Ruan, S. Zheng, Y. Yang, Z. Xiu, L. Li, C. Wu, Y. Gong, M. Yang and W. Lu, *Nat. Commun.*, 2024, **15**, 6138.

51 M. Yuan, A. H. Weible, F. Azadi, B. Li, J. Cui, H. Lv, R. Che and X. Wang, *Mater. Horiz.*, 2025, **12**, 1033–1057.

52 M. Yuan, B. Li, Y. Du, J. Liu, X. Zhou, J. Cui, H. Lv and R. Che, *Adv. Mater.*, 2025, **37**, 2417580.

53 Y. Zhao, R. Liu, K. Yao, S. Ye, Y. Guan, Y. Wu, X. Wang, Y. Rao, B. Yuan, W. Lu and Y. Yang, *Adv. Funct. Mater.*, 2025, e26207.

54 X. Guan, M. Jiang, Z. Shen, S. Tan, G. Ji and Z. J. Xu, *Adv. Funct. Mater.*, 2025, e27596.

55 S. Cheng, D. Sheng, S. Mukherjee, W. Dong, Y. Huang, R. Cao, A. Xie, R. A. Fischer and W. Li, *Nat. Commun.*, 2024, **15**, 9077.

56 Y. Yang, Z. Xiu, F. Pan, H. Liang, H. Jiang, H. Guo, X. Wang, L. Li, B. Yuan and W. Lu, *Adv. Funct. Mater.*, 2025, **35**, 2406133.

57 X. Wang, F. Pan, Z. Xiang, Q. Zeng, K. Pei, R. Che and W. Lu, *Carbon*, 2020, **157**, 130–139.

58 J. Liu, S. Tan, X. Yang, J. Zhu, X. Yan, T. Chen and G. Ji, *Nano-Micro Lett.*, 2026, **18**, 115.

59 P. Yi, X. Zhang, L. Jin, P. Chen, J. Tao, J. Zhou and Z. Yao, *Chem. Eng. J.*, 2022, **430**, 132879.

60 Y. Wu, S. Tan, T. Zhang, M. Zhou, G. Fang and G. Ji, *Nano Res.*, 2023, **16**, 8522–8532.

61 H. Zhao, Y. Cheng, Z. Zhang, J. Yu, J. Zheng, M. Zhou, L. Zhou, B. Zhang and G. Ji, *Composites, Part B*, 2020, **196**, 108119.

62 G. Peng, J. Zhou, J. Yao, L. Lu, J. Liu, K. Zou, J. Tao, Y. Liu and Z. Yao, *Carbon*, 2024, **229**, 119549.

63 H. Guan, Q. Wang, X. Wu, J. Pang, Z. Jiang, G. Chen, C. Dong, L. Wang and C. Gong, *Composites, Part B*, 2021, **207**, 108562.

64 W. Li, Z. Yu, Q. Wen, Y. Feng, B. Fan, R. Zhang and R. Riedel, *Int. Mater. Rev.*, 2023, **68**, 487–520.

65 J. Qiao, X. Zhang, C. Liu, L. Lyu, Y. Yang, Z. Wang, L. Wu, W. Liu, F. Wang and J. Liu, *Nano-Micro Lett.*, 2021, **13**, 75.

66 H. Wu, J. Liu, H. Liang and D. Zang, *Chem. Eng. J.*, 2020, **393**, 124743.

67 W. Song, M. Cao, Z. Hou, J. Yuan and X. Fang, *Scr. Mater.*, 2009, **61**, 201–204.

68 S. Wang, D. Li, Y. Zhou and L. Jiang, *ACS Nano*, 2020, **14**, 8634–8645.

69 D. Li, H. Liao, H. Kikuchi and T. Liu, *ACS Appl. Mater. Interfaces*, 2017, **9**, 44704–44714.

70 X. Zhang, Y. Rao, J. Guo and G. Qin, *Carbon*, 2016, **96**, 972–979.

71 Y. Li, X. Liu, X. Nie, W. Yang, Y. Wang, R. Yu and J. Shui, *Adv. Funct. Mater.*, 2019, **29**, 1807624.

72 Z. Lou, Q. Wang, U. I. Kara, R. S. Mamtani, X. Zhou, H. Bian, Z. Yang, Y. Li, H. Lv, S. Adera and X. Wang, *Nano-Micro Lett.*, 2022, **14**, 11.

73 J. Chen, J. Zheng, Q. Huang, G. Wang and G. Ji, *J. Mater. Sci. Technol.*, 2021, **94**, 239–246.

74 X. Liu, Y. Chen, X. Cui, M. Zeng, R. Yu and G. Wang, *J. Mater. Chem. A*, 2015, **3**, 12197.

75 M. Wu, Y. D. Zhang, S. Hui, T. D. Xiao, S. Ge, W. A. Hines, J. I. Budnick and G. W. Taylor, *Appl. Phys. Lett.*, 2002, **80**, 4404–4406.

76 A. Houbi, Z. A. Aldashevich, Y. Atassi, Z. B. Telmanovna, M. Saule and K. Kubanych, *J. Magn. Magn. Mater.*, 2021, **529**, 167839.

77 B. Wang, Q. Wu, Y. Fu and T. Liu, *J. Mater. Sci. Technol.*, 2021, **86**, 91–109.

78 Y. Liu, T. Cui, T. Wu, Y. Li and G. Tong, *Nanotechnology*, 2016, **27**, 165707.

79 M. Huang, L. Wang, K. Pei, B. Li, W. You, L. Yang, G. Zhou, J. Zhang, C. Liang and R. Che, *Adv. Funct. Mater.*, 2024, **34**, 2308898.

80 J. Hua, Z. Jiao, X. Han, J. Liu, M. Ma, J. Jiang, Y. Hou, X. Wang, C. Feng and Y. Ma, *J. Mater. Sci. Technol.*, 2024, **175**, 141–152.

81 Y. Li, K. Yun, X. Yi, C. Wang, X. Ding, S. Kang, D. Kong, J. Xing, K. Gao, B. Wang, K. Tian and R. Shu, *Carbon*, 2025, **244**, 120719.

82 J. Wang, H. Qu, X. Ye, S. Tan, X. Yan, P. Li, W. Tian and G. Ji, *J. Adv. Ceram.*, 2025, **14**, 9221191.

83 Q. Liu, Q. Cao, H. Bi, C. Liang, K. Yuan, W. She, Y. Yang and R. Che, *Adv. Mater.*, 2016, **28**, 486–490.

84 Z. Li, X. Li, Y. Zong, G. Tan, Y. Sun, Y. Lan, M. He, Z. Ren and X. Zheng, *Carbon*, 2017, **115**, 493–502.

85 R. Shu, J. Zhang, S. Liu and Z. Luo, *J. Mater. Chem. C*, 2023, **11**, 17012–17021.

86 Z. Fang, L. Peng, Y. Qian, X. Zhang, Y. Xie, J. J. Cha and G. Yu, *J. Am. Chem. Soc.*, 2018, **140**, 5241–5247.

87 K. Cao, T. Zoberbier, J. Biskupek, A. Botos, R. L. McSweeney, A. Kurtoglu, C. T. Stoppiello, A. V. Markevich, E. Besley, T. W. Chamberlain, U. Kaiser and A. N. Khlobystov, *Nat. Commun.*, 2018, **9**, 3382.

88 B. Li, Z. Ma, J. Xu, X. Zhang, Y. Chen and C. Zhu, *Small*, 2023, **19**, 2301226.

89 Z. Sun, Z. Yan, Z. Guo, H. Liu, L. Zhao and L. Qian, *Chem. Eng. J.*, 2023, **452**, 139430.

90 H. Xu, M. Liu, L. Huang, X. Zhang, Z. Ma, C. Zhu, F. Cao and Y. Chen, *Adv. Funct. Mater.*, 2025, **35**, 2502952.

91 X. Zhang, B. Li, J. Xu, X. Zhang, Y. Shi, C. Zhu, X. Zhang and Y. Chen, *Adv. Funct. Mater.*, 2023, **33**, 2210456.

92 Y. Lou, J. Li, X. Li, Z. Zhu, Z. Shi and B. Xu, *Nano Res.*, 2024, **17**, 6785–6794.

93 M. Huang, L. Wang, W. You and R. Che, *Small*, 2021, **17**, 2101416.

94 H. Liang, G. Chen, D. Liu, Z. Li, S. Hui, J. Yun, L. Zhang and H. Wu, *Adv. Funct. Mater.*, 2023, **33**, 2212604.

95 J. He, G. Zhang, Y. Xiao, C. Wang and N. Song, *J. Mater. Sci.: Mater. Electron.*, 2024, **35**, 354.

96 H. Liang, S. Hui, L. Zhang, K. Tao, Q. Chen, W. Lu and H. Wu, *Small*, 2025, **21**, 2408396.

97 R. Peymanfar, Z. S. Ershad, E. Selseleh-Zakerin and S. H. Tavassoli, *Ceram. Int.*, 2022, **48**, 16461–16476.

98 H. Lv, X. Zhou, G. Wu, U. I. Kara and X. Wang, *J. Mater. Chem. A*, 2021, **9**, 19170.

99 J. Tao, L. Xu, C. Pei, Y. Gu, Y. He, X. Zhang, X. Tao, J. Zhou, Z. Yao, S. Tao and H. Wu, *Adv. Funct. Mater.*, 2023, **33**, 2211996.

100 S. Tian, Z. Sun, H. Ding, Z. Guo, P. Wang, Y. Qiu, B. Du, J. Bi, G. Li and L. Qian, *Adv. Funct. Mater.*, 2024, **34**, 2310475.

101 G. Huang, S. Zhu, J. He, Q. Wu, Z. Jing, Y. Shen and N. Song, *App. Surf. Sci.*, 2025, **713**, 164308.

102 B. Fan, R. Ji, B. Huang, Y. Yu, C. Xie, Q. Lin, G. Tong, L. Xie and T. Wu, *Adv. Funct. Mater.*, 2025, **35**, e11825.

103 H. Wang, J. Xiao, X. Qi, X. Gong, J. Ding, Y. Qu, J. Yang and W. Zhong, *J. Mater. Sci. Technol.*, 2026, **247**, 55–63.

104 Y. Lu, X. Zhao, Q. Tian, Y. Lin, P. Li, Y. Tao, Z. Wang, J. Ma, H. Xu and Y. Liu, *Carbon*, 2024, **224**, 119083.

105 Y. Guan, R. Shu and B. Liu, *Chem. Eng. J.*, 2025, **505**, 159819.

106 F. He, W. Zhao, L. Cao, Z. Liu, L. Sun, Z. Zhang, H. Zhang and T. Qi, *Small*, 2023, **19**, 2205644.

107 J. Zhao, Z. Wang, H. Wang, P. Liu and R. Che, *Adv. Funct. Mater.*, 2025, **35**, 2418282.

108 H. Jia, Y. Duan, N. Wu, S. Gu, M. Wang, J. Di and J. Ma, *Chem. Eng. J.*, 2024, **496**, 153783.

109 C. Gong, J. Ding, C. Wang, Y. Zhang, H. Cong, H. Liu, Y. Guo, K. Song, C. Shi and F. He, *Chem. Eng. J.*, 2024, **480**, 147793.

110 Z. Hao, S. Shi, B. Wang, P. Liu, Q. Gao, K. Xu, Y. Ni, Z. Tian, W. Xiao, C. Zhu, G. Xu, H. Zhang and F. Liu, *J. Alloys Compd.*, 2025, **1024**, 180206.

111 Z. Su, S. Yi, W. Zhang, X. Xu, Y. Zhang, S. Zhou, B. Niu and D. Long, *Nano-Micro Lett.*, 2023, **15**, 183.

112 F. Zhang, N. Li, J. Shi, Y. Wang, D. Yan and Z. Li, *Small*, 2024, **20**, 2312135.

113 F. Gu, W. Wang, H. Meng, Y. Liu, L. Zhuang, H. Yu and Y. Chu, *Matter*, 2025, **8**, 102004.

114 Z. Qiu, X. Liu, T. Yang, J. Wang, Y. Wang, W. Ma and Y. Huang, *Adv. Funct. Mater.*, 2024, **34**, 2400220.

115 R. Xu, J. Zhou, W. Huang, G. Yu, L. Guo, X. Huang and G. Shao, *J. Mater. Chem. C*, 2024, **12**, 4640–4647.

116 H. Zhang, Z. Jia, B. Wang, X. Wu, T. Sun, X. Liu, L. Bi and G. Wu, *Chem. Eng. J.*, 2021, **421**, 129960.

117 T. Xiao, J. Kuang, H. Pu, Q. Zheng, Y. Lu, W. Liu and W. Cao, *J. Alloys Compd.*, 2021, **862**, 158032.

118 Y. Qiu, Y. Lin, H. Yang, L. Wang, M. Wang and B. Wen, *Chem. Eng. J.*, 2020, **383**, 123207.

119 Y. Sun, Y. Wang, D. Liu, H. Jiang, B. Ding, J. Guo and S. Dai, *ACS Appl. Mater. Interfaces*, 2025, **17**, 14278–14290.

120 Y. Liu, F. Wang, Y. Wang, B. Hu, P. Xu, X. Han and Y. Du, *Composites, Part B*, 2024, **273**, 111244.

121 L. Chen, J. Pan, T. Wang, W. Xia, J. He and K. Zhang, *Adv. Funct. Mater.*, 2025, **35**, 2409432.

122 B. Wang, H. Wu, W. Hou, Z. Fang, H. Liu, F. Huang, S. Li and H. Zhang, *J. Mater. Chem. A*, 2023, **11**, 23498–23510.

123 D. Shi, J. Zheng, Y. Qian, J. Liu, J. Zheng, J. Lv, W. Cai, L. Qiao, Y. Ying, J. Yu, J. Li and S. Che, *J. Alloys Compd.*, 2025, **1037**, 182377.

124 H. Lv, Y. Yao, S. Li, G. Wu, B. Zhao, X. Zhou, R. L. Dupont, U. I. Kara, Y. Zhou, S. Xi, B. Liu, R. Che, J. Zhang, H. Xu, S. Adera, R. Wu and X. Wang, *Nat. Commun.*, 2023, **14**, 1982.

125 S. Li, Y. Sun, K. Zhang, X. Jiang and H. Yu, *Small*, 2024, **20**, 2306990.

126 G. Liu, P. Zhu, J. Teng, R. Xi, X. Wang, X. Wang, M. Yan and C. Wu, *Adv. Funct. Mater.*, 2025, **35**, 2413048.

127 J. Wang, Y. Wang, R. Jiang, S. Chen, Q. He and G. Wu, *Mater. Today Phys.*, 2023, **35**, 101126.

128 S. Li, T. Ma, Z. Chai, Z. Zhang, M. Zhu, X. Tang, X. Zhao, Y. Lu, Q. Lan, Z. Wang, F. He, Z. Wang and T. Liu, *Carbon*, 2023, **207**, 105–115.

129 H. Lv, Y. Yao, M. Yuan, G. Chen, Y. Wang, L. Rao, S. Li, U. I. Kara, R. L. Dupont, C. Zhang, B. Chen, B. Liu, X. Zhou, R. Wu, S. Adera, R. Che, X. Zhang and X. Wang, *Nat. Commun.*, 2024, **15**, 1295.

130 Y. Tian, D. Estevez, G. Wang, M. Peng and F. Qin, *Carbon*, 2024, **218**, 118614.

131 Z. Jiao, W. Huyan, F. Yang, J. Yao, R. Tan, P. Chen, X. Tao, Z. Yao, J. Zhou and P. Liu, *Nano-Micro Lett.*, 2022, **14**, 173.

132 X. Su, J. Wang, T. Liu, Y. Zhang, Y. Liu, B. Zhang, Y. Liu, H. Wu and H. Xu, *Adv. Funct. Mater.*, 2024, **34**, 2403397.

133 T. Zhao, D. Lan, Z. Jia, Z. Gao and G. Wu, *Nano Res.*, 2024, **17**, 9845–9856.

134 X. Shi, Z. Wu, Z. Liu, J. Lv, Z. Zi and R. Che, *J. Mater. Chem. A*, 2022, **10**, 8807–8816.

135 F. Wang, N. Wang, X. Han, D. Liu, Y. Wang, L. Cui, P. Xu and Y. Du, *Carbon*, 2019, **145**, 701–711.

136 X. Jiang, Q. Wang, L. Song, H. Lu, H. Xu, G. Shao, H. Wang, R. Zhang, C. Wang and B. Fan, *Carbon Energy*, 2024, **6**, e502.

137 F. Dong, B. Dai, H. Zhang, Y. Shi, R. Zhao, X. Ding, H. Wang, T. Li, M. Ma and Y. Ma, *J. Colloid Interface Sci.*, 2023, **649**, 943–954.

138 Y. Liu, C. Tian, F. Wang, B. Hu, P. Xu, X. Han and Y. Du, *Chem. Eng. J.*, 2023, **461**, 141867.

139 Y. Zhang, Y. Li, M. Wei, D. Yang, Q. Zhang and B. Zhang, *J. Mater. Sci. Technol.*, 2022, **128**, 148–159.

140 Z. Wu, K. Pei, L. Xing, X. Yu, W. You and R. Che, *Adv. Funct. Mater.*, 2019, **29**, 1901448.

141 Q. Guo, F. Zhai, H. Wang, Y. Zhuang, X. Shao, T. Li, K. Xie and Y. Ma, *Chem. Eng. J.*, 2025, **520**, 165714.

142 H. Jiang, L. Huang, Y. Wei, B. Wang, H. Wu, Y. Zhang, H. Liu and S. Dou, *Nano-Micro Lett.*, 2019, **11**, 56.

143 Y. He, Q. Su, D. Liu, L. Xia, X. Huang, D. Lan, Y. Liu, Y. Huang and B. Zhong, *Chem. Eng. J.*, 2024, **491**, 152041.

144 Y. Yan, J. Zhou, J. Tao, L. Duan, Y. Liu, Z. Cheng, Y. Wang, Z. Liu, Z. Ning, X. Wang, X. Tao, P. Liu and Z. Yao, *Small*, 2025, **21**, 2410799.

145 B. Huang, J. Yue, B. Fan, Y. Liu and X. Huang, *Ceram. Int.*, 2022, **48**, 19375–19381.

146 L. Yan, C. Hong, B. Sun, G. Zhao, Y. Cheng, S. Dong, D. Zhang and X. Zhang, *ACS Appl. Mater. Interfaces*, 2017, **9**, 6320–6331.

147 J. Deng, H. Liu, Q. Cui, X. Zhang, L. Han, Q. He, Y. Wang, X. Yin and H. Li, *Carbon*, 2025, **244**, 120630.

148 Q. Su, D. Liu, C. Wang, L. Xia, X. Huang and B. Zhong, *ACS Appl. Nano Mater.*, 2022, **5**, 15902–15913.

149 Y. Du, Z. Yan, W. You, Q. Men, G. Chen, X. Lv, Y. Wu, K. Luo, B. Zhao, J. Zhang and R. Che, *Adv. Funct. Mater.*, 2023, **33**, 2301449.

150 G. Wang, C. Li, D. Estevez, P. Xu, M. Peng, H. Wei and F. Qin, *Nano-Micro Lett.*, 2023, **15**, 152.

151 S. Liu, Y. Lian, Y. Zhao, H. Hou, J. Ren, E. R. Elsharkawy, S. M. El-Bahy, Z. M. El-Bahy and N. Wu, *Adv. Compos. Hybrid Mater.*, 2025, **8**, 144.

152 J. Yang, J. Wang, H. Li, Z. Wu, Y. Xing, Y. Chen and L. Liu, *Adv. Sci.*, 2022, **9**, 2101988.

153 K. Cao, X. Yang, R. Zhao and W. Xue, *ACS Appl. Mater. Interfaces*, 2023, **15**, 9685–9696.

154 F. Wu, P. Hu, F. Hu, Z. Tian, J. Tang, P. Zhang, L. Pan, M. W. Barsoum, L. Cai and Z. Sun, *Nano-Micro Lett.*, 2023, **15**, 194.

155 C. Zhou, M. Yuan, X. Di, S. Qiu, M. Liang, Y. Luo and H. Zou, *Chem. Eng. J.*, 2025, **512**, 162574.

156 H. Zhang, K. Kuang, Y. Zhang, C. Sun, T. Yuan, R. Yin, Z. Fan, R. Che and L. Pan, *Nano-Micro Lett.*, 2025, **17**, 133.

157 D. Xiang, Q. He, C. Fan, Y. Wang, X. Yin and C. Wang, *Mater. Today Nano*, 2025, **30**, 100644.

158 S. Wu, C. Wang, Y. Tang, J. Jiang, H. Jiang, X. Xu, B. Cui, Y. Jiang and Y. Wang, *Adv. Fiber Mater.*, 2024, **6**, 430–443.

159 H. Gu, L. Tian, Q. Zhang, X. You, M. Wang, S. Dong and J. Yang, *Small*, 2024, **20**, 2402423.

160 Y. Deng, B. Ren, Y. Jia, Q. Wang and H. Li, *J. Mater. Sci. Technol.*, 2024, **196**, 50–59.

161 J. Zhang, X. Zhou, H. Wang, S. Li, H. Xi, P. Zhong, Z. Wang, J. Liu and H. Wu, *Carbon*, 2025, **244**, 120723.

162 S. Wang, Q. Liu, S. Li, F. Huang and H. Zhang, *ACS Nano*, 2024, **18**, 5040–5050.

163 J. Hu, J. Jiang, Q. Li, J. Cao, X. Sun, S. Huo, Z. Qin and Y. Pan, *Composites, Part A*, 2025, **198**, 109068.

164 S. Zhu, J. He, G. Huang, Y. Wang, P. Li, X. Wu, Y. Shang and N. Song, *Ceram. Int.*, 2025, **51**, 55897–55908.

165 M. Qiao, J. Li, D. Wei, X. He, X. Lei, J. Wei and Q. Zhang, *Microporous Mesoporous Mater.*, 2021, **314**, 110867.

166 C. Liu, L. Zhu, S. Zheng, L. Xu, L. Yan, Y. Zhang and G. Ji, *Acta Mater.*, 2025, **296**, 121255.

167 W. H. Choi, B. S. Kwak, J. H. Kweon and Y. W. Nam, *Compos. Struct.*, 2020, **238**, 111953.

168 W. Ma, X. Liu, T. Yang, J. Wang, Z. Qiu, Z. Cai, P. Bai, X. Ji and Y. Huang, *Adv. Funct. Mater.*, 2025, **35**, 2314046.

169 Z. Yang, F. Luo, W. Zhou, H. Jia and D. Zhu, *J. Alloys Compd.*, 2017, **699**, 534–539.

170 D. Zhang, Y. Chen and Q. Zhou, *Results Phys.*, 2025, **73**, 108261.

171 Z. Yang, W. Ren, L. Zhu, Y. Qing, Z. Huang, F. Luo and W. Zhou, *J. Alloys Compd.*, 2019, **803**, 111–117.

172 X. Li, D. Xu, D. Zhou, S. Pang, C. Du, M. A. Darwish, T. Zhou and S. Sun, *Carbon*, 2023, **208**, 374–383.

173 Y. Duan, B. Ma, L. Huang, X. Ma and M. Wang, *Adv. Mater. Technol.*, 2023, **8**, 2202172.

174 X. Deng, S. Gao, X. Qi, H. Dai, S. Fu, Q. Ni and Y. Fu, *Chem. Eng. J.*, 2023, **473**, 145040.

175 N. Wu, Y. Duan, W. Chen, Y. Shi, H. Jia, J. Ma and H. Pang, *Mater. Today Phys.*, 2025, **56**, 101766.

176 H. Sun, B. Yang and M. Zhang, *Adv. Fiber Mater.*, 2024, **6**, 1122–1137.

177 B. Huang, Y. Cao, F. Ye, J. Liang, C. Li and X. Fan, *J. Mater. Sci. Technol.*, 2026, **249**, 203–213.